Temporal and spatial dependence of hydrodynamic correlations: Simulation and experiment

Anthony J. C. Ladd*
Department of Theoretical and Applied Mechanics, Cornell University, Ithaca, New York 14853

Hu Gang
Exxon Research and Engineering Company, Route 22 East, Annandale, New Jersey 08801

J. X. Zhu
Department of Chemical Engineering, Princeton University, Princeton, New Jersey 07954

D. A. Weitz
Exxon Research and Engineering Company, Route 22 East, Annandale, New Jersey 08801
(Received 20 April 1995)

Time-dependent hydrodynamic interactions in a colloidal suspension of hard spheres are studied, both experimentally and through computer simulation. The focus is on the behavior at small wave vectors, which directly probes the temporal evolution of hydrodynamic interactions between nearby particles. The computer simulations show that the time-dependent diffusion coefficient has the same functional form for all wave vectors, with a single characteristic scaling time for each length scale and for each volume fraction. Wave-vector-averaged effective diffusion coefficients, measured experimentally using diffusing wave spectroscopy, also scale to the same functional form. In this case, the scaling time is dependent on both volume fraction and particle size; it decreases sharply with decreasing particle radius, reflecting the greater contribution from smaller wave vectors that is contained in the scattering from the smaller particles. For a direct comparison of simulation and experiment, we simulate the experimentally observed correlation functions, by averaging the wave-vector-dependent computer-simulation data with the weighting appropriate to the experimental technique. Although the overall scaling is similar, there are quantitative differences in the simulated and measured relaxation times. We suggest these differences are due to the compressibility of the suspension, and that the resultant pressure waves make an unexpectedly significant contribution to the hydrodynamic interactions.

PACS number(s): 82.70.Kj, 05.40.+j, 47.15.Pn, 82.70.Dd

I. INTRODUCTION

In this paper we report experimental and numerical studies of the spatial and temporal evolution of hydrodynamic interactions in colloidal suspensions of micron-sized spheres. When a sphere is set in motion by an external force or by a thermal fluctuation, it sets the surrounding fluid in motion by transferring momentum to it. Part of this momentum is carried off as sound waves, and spreads out in time over a spherical volume of radius $c_s t$ (c_s is the velocity of sound). The majority of the momentum transferred to the fluid diffuses throughout the system at a rate controlled by the kinematic shear viscosity of the fluid ν. Thus momentum that is initially localized near the particle spreads out over a spherical volume of radius $\sqrt{\nu t}$. This leads to a slow decay of the velocities of both the sphere and the surrounding fluid, which asymptotically vary as $(\nu t)^{-3/2}$ in three dimensions and as $(\nu t)^{-1}$ in two dimensions. In concentrated suspensions, the hydrodynamic flow fields interact with the solid particles giving rise to a complex, many-body scattering problem. These hydrodynamic interactions are ubiquitous to all particle-fluid suspensions. The aim of this work is to study the development of these hydrodynamic interactions, both in time and in space. We do this by investigating time-dependent correlations in particle motion, in dilute to concentrated suspensions, using a combination of light-scattering experiments and numerical simulation.

Since the colloidal particles are much larger than fluid molecules, there is a very large time scale separation between the diffusion of fluid momentum and the diffusion of particles; the ratio D/ν is of the order of 10^{-6}. Therefore there is a substantial time regime (typically between 10^{-8} and 10^{-5} s) during which the hydrodynamic flow fields and the particle velocities are evolving to a quasistationary state, whereas the particle coordinates are essentially fixed. Within this time range, we can study the temporal evolution of the hydrodynamic interactions without the added complications of changes in particle configuration. However, the experimental measurements must then probe particle motion over distances of order tens of angstroms. This can only be accomplished by using diffusing-wave spectroscopy (DWS), which is an extension of traditional dynamic light scattering into the multiple-scattering regime.

Dynamic light-scattering experiments measure the

phase shift between light scattered by different particles, via fluctuations in intensity of the scattered light; by time correlation, *relative* motion between particles can be detected [1]. However, single-scattering experiments can only observe motion on length scales of order 1000 Å, a significant fraction of a particle radius. By the time the particles have moved such distances (i.e., times of the order of milliseconds), the hydrodynamic interactions have long since reached the quasistatic or "creeping-flow" limit. Recently, a multiple-scattering technique, DWS, has been used to dramatically increase the spatial and temporal resolution of light-scattering experiments [2–4]. Diffusing-wave spectroscopy works because the phase shifts from each scattering event accumulate in a stochastic fashion, thereby increasing the resolution by the square root of the number of scattering events. In the strong-scattering limit, the photon path is purely diffusive and the experimental data can be deconvolved to obtain information about particle motions at very short length scales (10^{-8} cm in these experiments), and therefore, at very short times (10^{-8} s). However, each of the many scattering events along a particular photon path has a different scattering angle, between 0° and 180°; hence DWS probes an average over many different wave vectors [5], rather than a specific (and variable) wave vector as measured in a single-scattering experiment. Thus, while very short time scales can be resolved with DWS, the full spatial dependence of the hydrodynamic interactions cannot be determined.

To overcome this limitation of DWS, and to better understand the complex behavior of the hydrodynamic interactions, we use numerical simulations [6,7] as an important complement to the experimental data. These simulations provide the essential wave-vector-dependent resolution of the time-dependent hydrodynamic interactions. Our most important finding is that all the data, at any solid volume fraction, ϕ, and at any wave vector, q, can be scaled onto a single master curve [8]. The functional form of this curve corresponds to the time-dependent motion of a single suspended sphere, and can be calculated analytically. The data suggest that at a particular wavelength and volume fraction, the temporal evolution of hydrodynamic interactions is governed by a single relaxation time.

In order to directly compare the results of the numerical simulations with experimental DWS data, we have averaged the q-dependent simulation data over a range of wave vectors. We use a theoretically determined weighting factor that depends on the particle radius we wish to compare with, and the wavelength of the laser light. We find that the wave vector-averaged data also scale to the single-sphere curve; the relaxation time now depends on particle radius a (instead of wave vector) and volume fraction. Similar scaling is also seen experimentally. However, a significant discrepancy between the simulated and measured relaxation times persists; we suggest that this discrepancy actually reflects an important role that is played by sound waves, which carry a significantly larger fraction of the momentum in the experiment than in the simulations.

This paper is organized as follows. In the next section (II) the basic concepts of time- and space-dependent hydrodynamic interactions are introduced; we also discuss earlier results for both single-particle and collective diffusion. In Sec. III we present a theoretical description of the use of DWS to probe these highly concentrated, and therefore strongly scattering suspensions; this presentation emphasizes the physical concepts rather than the formal description. The experimental setup and the experimental results are described in the two subsequent sections (IV and V). In Sec. VI the simulation techniques are described and the key results are presented in Sec. VII. Section VII also includes a direct comparison between the simulation results and the experimental results; the observed discrepancies motivate a discussion of the effects of sound waves. The paper ends with a brief concluding section.

II. PREVIOUS RESULTS

A. Self-diffusion

It has been established, both experimentally [9,10] and by simulation [11], that the time evolution of the mean-square displacement of a tagged sphere, $\langle \Delta R^2(t) \rangle$, in a multiparticle suspension, can be characterized by a single relaxation time $\tau(\phi)$, at all solid volume fractions, ϕ. This scaling law is expressed in terms of the *hydrodynamic interaction function*

$$H(t) = \frac{1}{2D_0 t} \left\langle \frac{1}{3N} \sum_{i=1}^{N} \Delta R_i^2(t) \right\rangle ; \tag{1}$$

$D_0 = k_B T / 6\pi\eta_0 a$ is the diffusion coefficient of an isolated sphere of radius a in a solvent of viscosity η_0. All the experimental and numerical data for $H(t,\phi)$ can be fitted to a single master curve $H_0(t^*)$, which is a function of a reduced time $t^* = t/\tau$, and a volume-fraction dependent scaling time $\tau(\phi)$:

$$H(t,\phi) = H^{\infty}(\phi) H_0(t/\tau(\phi)), \tag{2}$$

where $H^{\infty}(\phi)$ is the long-time limit of $H(t,\phi)$. To avoid confusion, we point out that our long-time limit refers to the development of hydrodynamic interactions, rather than to the motion of the solid particles themselves. Thus $H^{\infty}(\phi)$ is related to short-time self-diffusion coefficient $D_S(\phi) = D_0 H^{\infty}(\phi)$. If the scaling relations described by Eq. (2) are to be valid at low concentrations, it follows that $\tau(0) = \tau_0 = \rho a^2/\eta_0$ and that $H_0(t^*)$ is the normalized mean-square displacement of an isolated sphere. If the fluid is assumed to be incompressible, then $H_0(t^*)$ is a known function of the reduced time and the ratio of the mass density of the solid particle to that of the fluid ρ_R [12]: its asymptotic expansions are

$$H_0(t^*) = \begin{cases} \frac{1}{2\alpha}t^* - \frac{8}{15\sqrt{\pi}\alpha^2}t^{*3/2} + O(t^{*2}), \\ \qquad\qquad t^* \ll 1\,, \qquad (3) \\ 1 - \frac{2}{\sqrt{\pi}}t^{*-1/2} + (1-\alpha)t^{*-1} + O(t^{*-3/2}), \\ \qquad\qquad t^* \gg 1\,; \qquad (4) \end{cases}$$

the parameter $\alpha = (2\rho_R + 1)/9$ includes the added-mass correction.

The experimental results [9] show that at higher volume fractions the time-dependent mean-square displacement has the same functional form as at low density, but with a relaxation time governed by the high-frequency viscosity of the suspension $\eta(\phi)$, rather than that of the pure fluid; i.e., $\tau(\phi) = \rho a^2/\eta(\phi)$. Thus in this picture, the suspension behaves as an effective fluid medium with a viscosity $\eta(\phi)$. However, additional experiments [10], probing an even shorter time regime, suggested that the scaling may extend to very short times $t/\tau < 1$. This is somewhat puzzling, in that these times are too short for hydrodynamic interactions to propagate over typical interparticle separations by viscous diffusion. Numerical simulations [11], incorporating accurate hydrodynamic interactions and thermal fluctuations, also found a scaling of the mean-square displacement over a very wide time regime, from reduced times $t/\tau = 0.1$ and up.

The simulations reproduced the experimentally observed scaling with acceptable accuracy; our earlier analysis [11] is reproduced in Fig. 1(a). However, the simulation data can actually be fitted more accurately by a slightly different time scaling $\tau(\phi) = H^\infty(\phi)\tau_0$, as shown in Fig. 1(b); thus the scaling time is proportional here to the self-diffusion coefficient, rather than the inverse of the viscosity. If the time dependence of the hydrodynamic interactions is a single relaxation process, as suggested by the scaling relation described by Eq. (2), then we would expect that the velocity autocorrelation function,

$$J(t) = \left\langle \frac{1}{3N}\sum_{i=1}^{N} \mathbf{U}_i(t)\cdot\mathbf{U}_i(0) \right\rangle = \frac{d^2}{dt^2}\left[D_0 t H(t)\right], \quad (5)$$

will also scale with the same volume-fraction-dependent relaxation time [13]. According to Eq. (2),

$$J(t,\phi) = \frac{k_B T}{M}\frac{H^\infty(\phi)\tau_0}{\tau(\phi)}\, J_0(t/\tau(\phi)), \qquad (6)$$

where M is the particle mass and $J_0(t^*)$ is the velocity correlation function for an isolated sphere,

$$J_0(t^*) = \left(\alpha - \frac{1}{9}\right)\frac{d^2}{dt^{*2}}\left[t^* H_0(t^*)\right]. \qquad (7)$$

The asymptotic expansions of $J_0(t^*)$ are

$$J_0(t^*) = \begin{cases} \left(1 - \frac{1}{9\alpha}\right)\left(1 - \frac{2}{\sqrt{\pi}\alpha}t^{*1/2}\right) + O(t^*), \qquad (8) \\ \qquad\qquad t^* \ll 1\,; \\ \left(\alpha - \frac{1}{9}\right)\frac{1}{2\sqrt{\pi}}t^{*-3/2} + O(t^{*-5/2}), \\ \qquad\qquad t^* \gg 1\,. \qquad (9) \end{cases}$$

It can be seen that at short times $J_0(t^*)$ does not asymptote to unity but to a smaller quantity $(1 + 1/2\rho_R)^{-1}$. This is a consequence of the incompressible fluid model, used to derive the expression for $H_0(t)$; it neglects the part of the initial momentum that is carried off by sound waves. It is *assumed* that this initial relaxation is so rapid that it makes a negligible contribution to the mean-square displacement. While this is clearly true for an

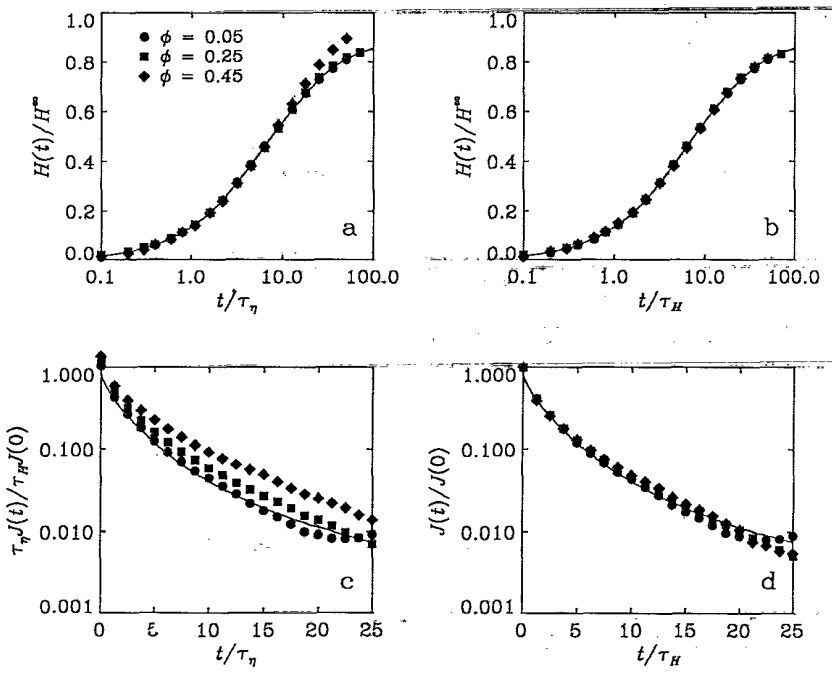

FIG. 1. Density-dependent scaling of the single-particle hydrodynamic correlations. Simulations of the scaled mean-square displacement $H(t)/H^\infty$ are plotted with two different time scalings: $\tau_\eta = \rho a^2/\eta(\phi)$ and $\tau_H = H^\infty \rho a^2/\eta_0$. Also shown are the velocity autocorrelation functions under the same time scaling, normalized to give the correct self-diffusion coefficient (or H^∞) upon integration.

isolated sphere, the situation in a dense many-body suspension is more complex. We will return to this point in Sec. VII D.

It is clear from Eq. (6) that the velocity correlation functions will *not* scale to a single curve unless the relaxation time is proportional to $H^\infty(\phi)$; i.e., $\tau(\phi) = H^\infty(\phi)\tau_0$. Thus it is interesting that precisely this scaling produces the best fit to the simulation data; the scaled velocity correlation functions are shown in Figs. 1(c) and 1(d). The simulation data [scaled as in Figs. 1(b) and 1(d) by $H^\infty(\phi)\tau_0$] imply that there is a single relaxation process, so that a scaled velocity correlation function can be integrated to give a mean-square displacement with similar scaling. This is not true of the experimentally measured $H(t)$ data [9]; they clearly scale better using the inverse of $\eta(\phi)$ rather than $D_S(\phi)$. Thus, it would not be possible to generate a scaled set of velocity correlation functions by just differentiating the scaled experimental $H(t)$ data with respect to time [Eqs. (6) and (7)]. This suggests that there may be an additional relaxation process in the experiments that is absent from the simulations. One possible cause is the different mass density ratios of solid particles and fluid. Experimentally $\rho_R \approx 1$, whereas in the simulations (for computational reasons, discussed in Sec. VI) ρ_R is usually around 10 and in all cases at least 5. If sound waves do make a significant contribution to the mean-square displacements in dense suspensions of neutrally buoyant particles, then we might expect a noticeable difference in relaxation times when compared with more massive particles used in the simulations, for which the sound-wave contributions would be much smaller. This is discussed in more detail later in the paper (Sec. VII D).

B. Collective diffusion

We investigate the spatial dependence of hydrodynamic interactions by probing a wave-vector-dependent analogue of the mean-square displacement, $H(q,t)$:

$$H(q,t) = \frac{1}{2D_0 t}\left\langle \frac{1}{N}\sum_{i,j=1}^{N} \hat{\mathbf{q}}\cdot[\mathbf{R}_i(t)-\mathbf{R}_i(0)] \times [\mathbf{R}_j(t)-\mathbf{R}_j(0)]\cdot\hat{\mathbf{q}}\, e^{i\mathbf{q}\cdot\mathbf{R}_{ij}}\right\rangle, \quad (10)$$

where $\hat{\mathbf{q}} = \mathbf{q}/q$ and $\mathbf{R}_{ij} = \mathbf{R}_i - \mathbf{R}_j$. For large values of q, terms with $i \neq j$ average to zero; in this limit the time-dependent hydrodynamic interaction function $H(q,t)$ reduces to the one-particle interaction function $H(t)$, which is independent of q. At longer wavelengths (smaller q) collective motions make important contributions to $H(q,t)$. Thus, it is useful to decompose $H(q,t)$ into the sum of $H(t)$ and an interaction contribution $H_I(q,t)$;

$$H(q,t) = H(t) + H_I(q,t). \quad (11)$$

The interaction contribution $H_I(q,t)$ consists exclusively of the terms with $i \neq j$ and directly measures the effects of interparticle hydrodynamic interactions; it shows how the trajectory of one particle is affected by the motion of its neighbors. By examining how the time evolution of $H_I(q,t)$ varies with q, we can begin to understand the spatial dependence of hydrodynamic interactions as well as the time dependence.

In the DWS experiments, it is not possible to measure $H(q,t)$ directly; instead what is measured is a weighted average over a range of wave vectors, denoted by $[H(t)]$. The weighting function that determines $[H(t)]$ depends on the particle radius a (see Sec. III); thus, by varying the particle size, different ranges of wave vector can be probed. Surprisingly, the same scaling of $[H(t)]$ data, which was previously observed for large particles [9], is reproduced for small particles as well [8]. The interesting implication of this result is that the collective hydrodynamic interactions, $H(q,t)$, must scale in a similar way to the single-particle interactions. To verify this supposition we have used computer simulations to calculate $H(q,t)$ directly, rather than the weighted average over q determined by DWS. Scaling *is* observed in the numerical simulations at each individual q; $H(q,t)$ can be scaled onto the single-particle curve, with a scaling time, $\tau(q,\phi)$, that depends on both q and ϕ. The q dependence of the scaling time is similar to $H^\infty(q,\phi)$.

To compare the simulation results more directly with experiment, we have averaged the simulated $H(q,t)$ over different q values, using a theoretically determined weighting function for each particle radius that matches the expected DWS weighting. We find a rather large discrepancy between the measured and predicted relaxation times, factors of 2 or more [8]. The differences in the single-particle (large-sphere) scaling times are not as large, about 35% at $\phi = 0.45$, and could even be explained by the combined uncertainties in the simulations and experiments. However, the differences in the scaling times for collective diffusion (small spheres) are too large to be accounted for by experimental uncertainty; we speculate that both discrepancies have the same physical origin, resulting from the effects of momentum transported away by the sound waves.

III. DIFFUSING WAVE SPECTROSCOPY OF OPTICALLY INTERACTING PARTICLES

The key assumption in interpreting the results of a DWS experiment is that the propagation of light through the scattering medium can be described by a diffusion equation [2,14]. Thus the photon paths through the scattering volume are described by a random walk; the distribution of these paths is determined by a solution of the diffusion equation for the experimental geometry. Each photon path is ascribed a phase, which evolves in time with the motion of the scattering particles that comprise the path. Moreover, since each path is comprised of a different set of scattering particles, these paths are statistically uncorrelated. Thus, the field correlation function from each path can be calculated individually and the total correlation function is just the sum of the contri-

butions from the individual paths, weighted by the probability that a diffusing photon follows that path. The correlation function of each path is calculated by summing the contributions of all the scattering events which make up the path. Since the light must scatter a large number of times in traversing the sample, the contributions of the individual scattering events are averaged over all scattering angles, with a weighting factor determined by the angular scattering probability of the light.

The interpretation of DWS data is more complex than in the case of single-scattering experiments. To show how the data can be interpreted to extract information about particle motion, we present a summary of the theory of DWS for optically interacting particles [15,16]. Our derivation is motivated by a physical picture for the multiple-scattering process, and explicitly demonstrates how DWS experiments probe an average of $H(q,t)$ as defined in Eq. (10). We obtain the same results as other less specific derivations [15], as well as more formal diagrammatic techniques [17]. Before proceeding with the more complicated calculation for multiply scattered light, it is instructive to consider the case of singly scattered light in order to indicate how $H(q,t)$ [Eq. (10)] can be determined from a light-scattering measurement.

In the weak-scattering limit, the scattered electric field from a suspension of identical particles is given by the sum of the scattered fields from each particle:

$$E(q,t) = b(q) \sum_{i=1}^{N} e^{-i\mathbf{q}\cdot\mathbf{R}_i(t)}; \tag{12}$$

here we neglect q-independent constants that will cancel in the normalization. The scattering amplitude $b(q)$ is related to the form factor of a particle,

$$F(q) = b(q)b^*(q). \tag{13}$$

The interpretation of dynamic light-scattering experiments follows from the normalized electric-field autocorrelation function [18]

$$g_1(t) = \frac{\langle E(0)E^*(t)\rangle}{\langle E(0)E^*(0)\rangle} = \frac{S(q,t)}{S(q)}, \tag{14}$$

where the dynamic structure factor is defined by

$$S(q,t) = \left\langle \frac{1}{N} \sum_{i,j=1}^{N} e^{i\mathbf{q}\cdot[\mathbf{R}_i(t)-\mathbf{R}_j(0)]} \right\rangle. \tag{15}$$

The static structure factor, $S(q) = S(q,0)$, reflects the coherence of light scattered by particles whose positions are correlated and which lie within a volume of order q^{-3}; the dynamic structure factor reflects the temporal decay of these correlations. A schematic representation of the contributions to the structure factor is illustrated in Fig. 2(a). The lines represent the path of light scattered from each particle at a given $\mathbf{q}$. Light scattered from particles within the correlated region is coherent (or at least has a coherent contribution); thus the fields scattered from each of the correlated particles must be added in order to calculate the total scattered intensity. However, particles outside the correlation volume do not scatter coherently with those inside it; on average, the randomness of the phases causes their scattered fields to cancel, so they make no contribution. Thus the total scattered intensity is an incoherent summation of contributions from each correlation volume. The scattering from each correlation volume is again proportional to the dynamic structure factor, but summed over only the N_ξ particles within that volume,

$$S(q,t) = \left\langle \frac{1}{N_\xi} \sum_{i,j=1}^{N_\xi} e^{i\mathbf{q}\cdot[\mathbf{R}_i(t)-\mathbf{R}_j(0)]} \right\rangle. \tag{16}$$

We will use this result below.

We can express $g_1(t)$ in terms of $H(q,t)$ by making use of the relation [19]

$$\frac{d^2}{dt^2}\langle \mathbf{A}(t)\cdot\mathbf{A}^*(0)\rangle = -\left\langle \dot{\mathbf{A}}(t)\cdot\dot{\mathbf{A}}^*(0)\right\rangle : \tag{17}$$

substituting the dynamic structure factor into Eq. (17),

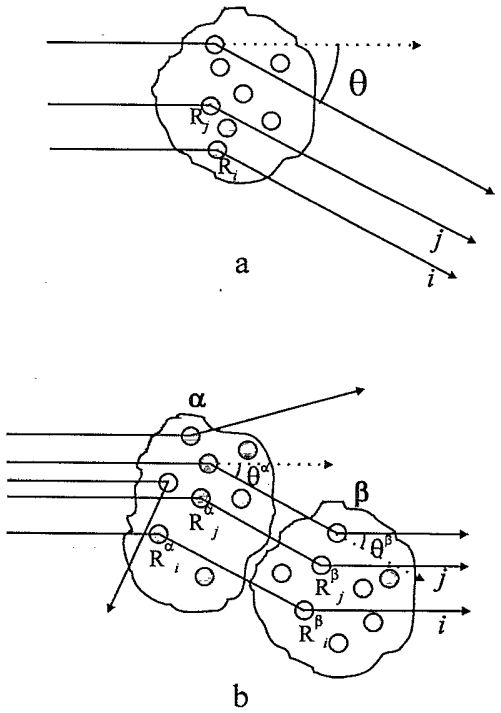

FIG. 2. Schematic representation of the scattering paths that lead to the dynamic structure factor for (a) single light scattering, and (b) multiple light scattering. These paths must be added coherently to calculate the correlation function of the scattered field. In the case of multiple scattering, the contribution of the paths labeled i and j must be added coherently; the contribution from each correlation volume, labeled as α and β, is the same as the dynamic structure factor for single scattering, averaged over all scattering directions. The scattering angle for a single scattering event θ is shown in (a), while the scattering angles for multiple scattering, θ^α and θ^β, are shown in (b).

we obtain the relation

$$\frac{d^2}{dt^2}S(q,t) = -q^2\left\langle \frac{1}{N}\sum_{i,j=1}^{N} \hat{\mathbf{q}}\cdot\mathbf{U}_i(t)\hat{\mathbf{q}}\cdot\mathbf{U}_j(0) \times e^{i\mathbf{q}\cdot[\mathbf{R}_i(t)-\mathbf{R}_j(0)]}\right\rangle, \quad (18)$$

where $\mathbf{U}_i(t)$ is the velocity of the ith particle. In single-scattering experiments, particle motion can only be detected at relatively long times, when the velocity correlation function has decayed to zero. By contrast, in a DWS experiment the times are so short that the particles have not moved a significant distance compared with the wavelength of light; thus we can ignore the time dependence of the phase factor, and approximate Eq. (18) by

$$\frac{d^2}{dt^2}S(q,t) = -q^2\left\langle \frac{1}{N}\sum_{i,j=1}^{N} \hat{\mathbf{q}}\cdot\mathbf{U}_i(t)\hat{\mathbf{q}}\cdot\mathbf{U}_j(0)e^{i\mathbf{q}\cdot\mathbf{R}_{ij}}\right\rangle. \quad (19)$$

Integrating Eq. (19) twice with respect to time, we obtain an expression for the structure factor that is valid for small particle displacements,

$$S(q,t) = S(q)\left[1-\frac{q^2}{2S(q)}\left\{\frac{1}{3N}\sum_{i=1}^{N}\langle\Delta R_i^2(t)\rangle + \left\langle\frac{1}{N}\sum_{i\neq j=1}^{N}\hat{\mathbf{q}}\cdot\Delta\mathbf{R}_i(t)\hat{\mathbf{q}}\cdot\Delta\mathbf{R}_j(t)e^{i\mathbf{q}\cdot\mathbf{R}_{ij}}\right\rangle\right\}\right], \quad (20)$$

where $\Delta\mathbf{R}_i(t) = \mathbf{R}_i(t) - \mathbf{R}_i(0)$. The two terms in braces are proportional to the self and interaction parts of $H(q,t)$, respectively [Eq. (11)]. Using the definition of the q-dependent hydrodynamic interaction function $H(q,t)$ [Eq. (10)], Eq. (20) can be rewritten as

$$S(q,t) = S(q)\left[1-\frac{q^2D_0H(q,t)t}{S(q)}\right]. \quad (21)$$

We note that this form is similar to the traditional expansion of the dynamic structure factor in terms of a collective, q-dependent diffusion coefficient [19],

$$S(q,t) = S(q)e^{-q^2D(q)t} \approx S(q)\left[1-\frac{q^2D_0H(q)t}{S(q)}\right]; \quad (22)$$

here, the hydrodynamic interaction function, $H(q)$, is q dependent, but not time dependent, since it describes light-scattering experiments that are insensitive to the time evolution of the hydrodynamic interactions. By contrast, we have now included an explicit time dependence to account for the temporal evolution of the hydrodynamic interactions.

To extend this treatment to the case of multiple scattering, we must calculate the correlation function for a typical diffusive light path. The scattered field from a single path with n scattering events is the product of the scattered fields from each event,

$$E^n(t) = \prod_{\alpha=1}^{n} b(q^\alpha)e^{i\mathbf{q}^\alpha\cdot\mathbf{R}^\alpha(t)}; \quad (23)$$

$\mathbf{q}^\alpha$ is the scattering vector for the event α, and $\mathbf{R}^\alpha$ is the particle involved in this scattering event. However, each of these α scattering events is coherently correlated with scattering events from some neighboring particles; this results in a correlation between adjacent diffusive paths. Thus, we must coherently add the scattered fields from correlated paths, and the total scattered field of this nth-order scattering sequence is [16]

$$E^n(t) = \sum_{i=1}^{N_\xi}E_i^n(t) = \sum_{i=1}^{N_\xi}\prod_{\alpha=1}^{n} b(q_i^\alpha)e^{i\mathbf{q}_i^\alpha\cdot\mathbf{R}_i^\alpha(t)}; \quad (24)$$

here the subscript i refers to one of the N_ξ correlated scattering paths. We schematically illustrate these coherent scattering paths in Fig. 2(b), where we show the contributions from two adjacent correlation volumes, α and β. The paths labeled i and j scatter from particles within each of the correlation volumes and must, therefore, be added coherently. The other scattering paths shown do not follow a path that retains their coherence, and therefore need not be added coherently. Thus, the time-dependent field correlation function for nth-order scattering sequences that maintain their coherence is

$$G_1^n(t) = \langle E^n(t)E^{n*}(0)\rangle = \left\langle\sum_{i,j=1}^{N_\xi}\prod_{\alpha,\beta=1}^{n} b(q_i^\alpha)b(q_j^\beta)e^{i\mathbf{q}_i^\alpha\cdot\mathbf{R}_i^\alpha(t)-i\mathbf{q}_j^\beta\cdot\mathbf{R}_j^\beta(0)}\right\rangle. \quad (25)$$

To simplify this expression, we consider the many scattering paths within the αth scattering event. To remain fully correlated, these individual paths must follow very nearly the same route; thus we approximate the scattering wave vectors within the event, but for different paths, as being equal, so that $\mathbf{q}_i^\alpha = \mathbf{q}_j^\alpha$. In addition, we make the further assumption that only one scattering event can occur in each correlation volume; this requires that the scattering mean free path l is greater than the correlation length ξ, which is of the order of a few particle diameters. This places a limit on the degree of multiple scattering; there should not be more than one scattering event in each correlated volume. With these assumptions, particles from different scattering events are not correlated in time, and terms with $\alpha \neq \beta$ average to zero; thus

$$G_1^n(t) = \left\langle\prod_{\alpha=1}^{n}F(q^\alpha)\sum_{i,j=1}^{N_\xi}e^{i\mathbf{q}^\alpha\cdot[\mathbf{R}_i^\alpha(t)-\mathbf{R}_j^\alpha(0)]}\right\rangle. \quad (26)$$

Here the summation extends over each correlation volume that contains N_ξ particles. We can identify this summation as the dynamic structure factor for the αth scattering event, Eq. (16). Thus we can simplify Eq. (26) to

$$G_1^n(t) = \left\langle \prod_{\alpha=1}^{n} F(q^\alpha) N_\xi S(q^\alpha, t) \right\rangle. \tag{27}$$

Equation (27) relates the contribution of the correlation function from a diffusive light path to the dynamic structure factor that is measured in a single-scattering experiment. The essential approximation is that only a single scattering event occurs within a correlation volume; the multiple scattering results from the transport of the light through many independent correlation volumes. We assume that the scattering events from the different correlation volumes are statistically independent, and that there are a sufficient number of them that we can neglect the details of the momentum conservation between each scattering event in any path.

The ensemble average in Eq. (27) ensures that each scattering event includes contributions from many different paths. Thus each of the α scattering events in Eq. (27) can be replaced by an average over all possible scattering vectors,

$$\frac{N_\xi \int_0^{2k_0} qF(q)S(q,t)dq}{\int_0^{2k_0} qdq}.$$

The integral extends over all possible scattering angles from 0 to 180°, corresponding to the limits $q = 0$ and $q = 2k_0$; k_0 is the wave vector of the incoming light. The form factor $F(q)$ determines the relative weighting at each value of q; in addition, averaging over all possible scattering angles θ (see Fig. 2) introduces a further factor of q ($q = 2k_0 \sin\theta$). In terms of the average scattering,

$$G_1^n(t) = \left[\frac{N_\xi}{2k_0^2} \int_0^{2k_0} qF(q)S(q,t)dq \right]^n, \tag{28}$$

and the normalized correlation function for an nth-order sequence is therefore

$$g_1^n(t) = \frac{\left[\int_0^{2k_0} qF(q)S(q,t)dq\right]^n}{\left[\int_0^{2k_0} qF(q)S(q)dq\right]^n}. \tag{29}$$

Using the short time expansion of $S(q,t)$, Eq. (21), we obtain

$$g_1^n(t) = \left[1 - \frac{D_0 t \int_0^{2k_0} q^3 F(q)H(q,t)dq}{\int_0^{2k_0} qF(q)S(q)dq}\right]^n = \exp\left\{-nD_0 t \frac{\int_0^{2k_0} q^3 F(q)H(q,t)dq}{\int_0^{2k_0} qF(q)S(q)dq}\right\}. \tag{30}$$

In order to describe the multiple scattering by a diffusion equation, we must express $g_1^n(t)$ [Eq. (30)] in terms of the path length of the scattered light $s = nl$, where l is the mean free path between scattering events [15]. However, the direction of a photon is not completely randomized by a single scattering event; instead there is a persistence in direction over a longer distance, the transport mean free path, l^* [20]. In terms of the scattering angle θ (see Fig. 2),

$$l^* = \frac{l}{1 - \langle\cos\theta\rangle}; \tag{31}$$

this is analogous to the persistence length of a semirigid polymer chain [21]. The scattering angle θ is geometrically related to k_0 and q by $1 - \cos\theta = q^2/2k_0^2$; therefore

$$\frac{l^*}{l} = \frac{2k_0^2}{\langle q^2\rangle} = 2k_0^2 \frac{\int_0^{2k_0} qF(q)S(q)dq}{\int_0^{2k_0} q^3 F(q)S(q)dq}. \tag{32}$$

Thus the correlation function for an nth-order scattering sequence, $g_1^n(t)$, can be expressed in terms of the contour length s of the scattering path and the *transport* mean free path l^* [22],

$$g_1^n(t) = \exp\left\{-2D_0 t k_0^2 \frac{s}{l^*} \frac{[H(t)]}{[S]}\right\}. \tag{33}$$

The average of $H(q,t)$ measured by DWS, $[H(t)]$, is given by [22]

$$[H(t)] = \frac{\int_0^{2k_0} q^3 F(q)H(q,t)dq}{\int_0^{2k_0} q^3 F(q)dq}; \tag{34}$$

the square brackets around S indicate the same average over q. The transport mean free path, l^*, is the characteristic length for photon diffusion; s/l^* is the number of steps in a random walk that is statistically equivalent to the photon path. Thus the total field correlation function is [5,15]

$$g_1(t) = \int_0^\infty P(s) \exp\left\{-2D_0 t k_0^2 \frac{s}{l^*} \frac{[H(t)]}{[S]}\right\} ds, \tag{35}$$

where $P(s)$ is the probability that diffusing photons follow a path of length s; it is calculated by solving the diffusion equation for the light, in the experimental geometry, subject to appropriate initial and boundary conditions. We can rewrite Eq. (35) in terms of a reduced time,

$$t_D^* = 2D_0 k_0^2 \frac{[H(t)]}{[S]} t, \tag{36}$$

and a reduced contour length, $s^* = s/l^*$;

$$g_1(t_D^*) = \int_0^\infty P(s^*) e^{-s^* t_D^*} ds^*. \tag{37}$$

The solution of Eq. (37) has been discussed extensively

elsewhere [14,23]; it depends on the experimental geometry. In this work the sample is a slab of thickness L, and of essentially infinite lateral extent. A transmission geometry is used; the incident light is focused on one side of the sample, and the scattered light is collected from a point on the other side of the sample. The correlation function is given by [23]

$$g_1(t) = \int_{\sqrt{3t_D^*}L/l^*}^{\infty} \left\{ A(s) \sinh s^* + e^{-s^*\left(1-\frac{4l^*}{3L}\right)} \right\} ds^*, \tag{38}$$

where

$$A(s^*) = \frac{\left(\frac{2l^*}{3L}s^* - 1\right)\left\{\frac{2l^*}{3L}e^{\frac{4s^*l^*}{3L}} + \left(\sinh s^* + \frac{2s^*l^*}{3L}\cosh s^*\right)e^{s^*\left(1-\frac{4l^*}{3L}\right)}\right\}}{\left(\sinh s^* + \frac{2s^*l^*}{3L}\cosh s^*\right)^2 - \left(\frac{2s^*l^*}{3L}\right)^2}. \tag{39}$$

These equations provide an excellent description of the correlation functions obtained from DWS experiments in the transmission geometry, as has been confirmed by studies of optically noninteracting particles [5]. Assuming that the data are described by these equations, a zero crossing routine can be used to invert the data and obtain t_D^* from the lower limit of the integral in Eq. (38). Then we can determine the time evolution of $[H(t)]$ through Eq. (36). The transport mean free path of the light, l^*, can be determined through another experimental measurement such as the total transmission, or by a theoretical calculation.

Even with the averaging over q inherent in DWS, it is still possible to obtain information about the q dependence of hydrodynamic interactions, by studying the scattering from particles of different sizes [8]. The relevant parameter is the product qa; thus the upper limit of integration in Eq. (34) is effectively $2k_0a$. Physically, this reflects the fact that the scattering dynamics are sensitive to the number of particles in a volume of order q^{-3}. If

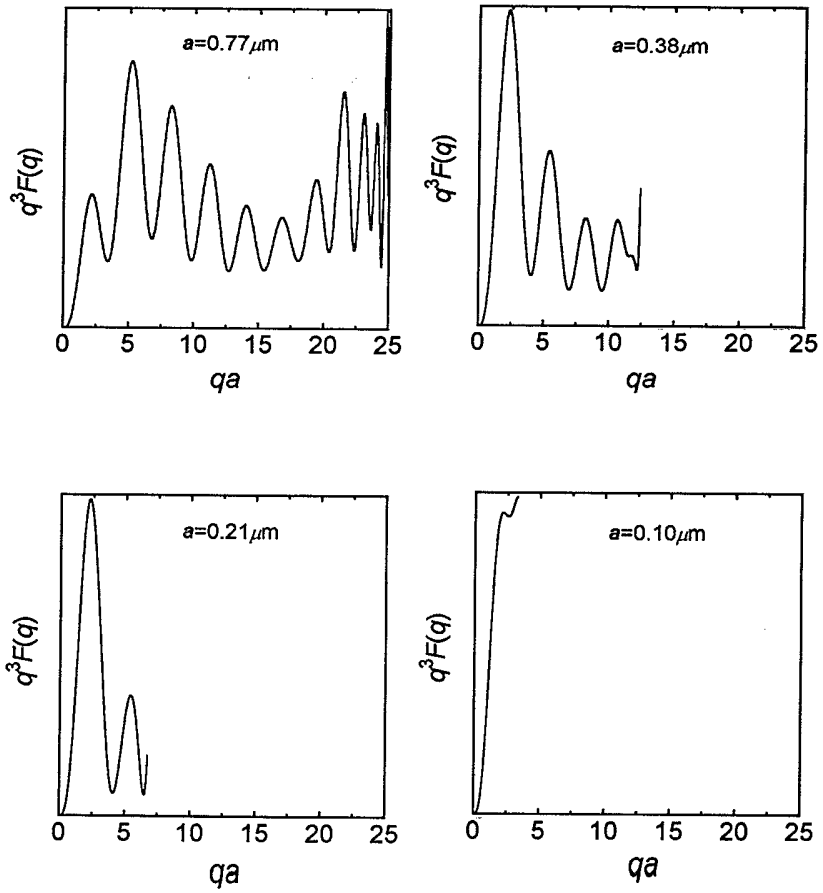

FIG. 3. The weighting factors used for the DWS averaging for the different sphere sizes. The data are plotted in arbitrary units, as a function of qa. The weights for the larger spheres emphasize the large qa region, and thus reflect the self-diffusion of the particles. By contrast, the weights for the smaller spheres emphasize values of qa below the first peak in the structure factor, and thus reflect the effects of interparticle interactions.

large particles are used, only a single particle can fit into this volume, and most of the contribution to the average arises from values of $qa > 1$. Then the DWS measurement reflects the high-q limit of $H(q,t)$, corresponding to the time-dependent self-diffusion coefficient $H(t)$. By contrast, if smaller particles are used, more than a single particle can fit into this volume, and the average reflects increasing contributions from values of $qa \leq \pi$, so that $H_I(q,t)$ makes a larger contribution.

The effects of using different size particles can be seen more quantitatively by examining the weighting factor in Eq. (34), $q^3F(q)$. The overall q^3 factor arises from two contributions; a factor of q arises from the phase space available for scattering, while the remaining factor of q^2 arises because of the diffusive dynamics. The q^3 factor ensures that the dominant contribution to the average arises from the larger values of q. We plot $q^3F(q)$ as a function of qa in Fig. 3, for several of the particle sizes used in our experiments. The form factors were calculated using Mie theory [24], and the results for each particle size were normalized by their maximum value. The weighting factors are plotted to the maximum value of qa in each case, i.e., $2k_0a$, where $k_0 = 16.24\ \mu\text{m}^{-1}$. The strong oscillations reflect the Mie resonances in the form factor. For the larger particles, the dominant contribution to the integral in Eq. (34) comes from values of qa greater than the first peak in the structure factor ($qa = \pi$); as a result the integral reflects the self-contribution, $H(t)$, only. By contrast, for the smallest particles, all of the weight in the integral arises from values of qa less than the first peak of the structure factor, making the contribution of collective effects much more important, so that in this case $H_I(q,t)$ makes a significant contribution.

IV. EXPERIMENTAL METHOD

Our samples are aqueous suspensions of highly monodisperse polystyrene latex spheres. These particles are stabilized against aggregation by charges adsorbed on their surface; their Coulombic repulsion prevents the particles from touching when they approach one another. The range of this repulsive interaction is determined by the screening length, which is set by the total concentration of charges in the solution. Since the screening length is much smaller than the particle radius, the particle-particle interactions closely approximate those of hard spheres. We estimate that the screening length is roughly 50 Å, compared with a typical particle radius of 1 μm; for the smallest particles (radius 0.1 μm), we add additional acid to the solution to reduce the screening length still further, and ensure that it remains much less than the particle size. We believe that the particle positions, as reflected by the pair correlation function, $g(r)$, are very well characterized by the hard-sphere distribution. However, there is a possibility that the interactions between the particles will be affected by the slightly softened potential caused by the finite range of the screened Coulombic repulsion. This will be increasingly likely for the smaller particles, where the screening length becomes a more appreciable fraction of the radius. Although we cannot rule out this possibility completely, we have no direct evidence for it.

The radii of the particles studied included 0.099, 0.206, 0.380, 0.765, and 1.55 μm; the precise values were determined by dynamic light-scattering measurements of the hydrodynamic radius, performed at very low concentrations. This range in particle size allows us to probe both the high-q, single-particle limit of $H(q,t)$ (using the larger spheres), as well as collective motions at smaller qa (using the smaller spheres). There is a lower limit to the particle size; particles smaller than 0.1 μm do not scatter strongly enough to enable the diffusion approximation, inherent in DWS, to be used. The samples were initially prepared in a stock solution with $\phi = 0.10$. Lower concentrations were prepared by diluting with water to the desired concentration. Higher concentrations were prepared by sedimentation, using gravity for the larger spheres or a centrifuge for the smaller spheres. Water was removed from the top of the sediment to attain the desired volume fraction and the samples were remixed. In all cases the volume fraction was measured directly by weighing a portion of the sample before and after drying in a vacuum oven, maintained at room temperature. The weight fractions were converted to volume fractions by assuming that the particle density was equal to the density of bulk polystyrene.

A schematic of the experimental setup is shown in Fig. 4. The laser was an Ar^+ ion laser, operating at a wavelength of 0.5145 μm. A temperature-controlled etalon in the laser cavity forced it to operate on a single longitudinal mode. This was essential because our detection system was sufficiently fast to be able to detect the beats between neighboring modes, which occurred at 125 MHz for our laser cavity. Moreover, operating in a single mode ensures that the temporal correlation length of the light is larger that the longest diffusive light paths in the sample. If this is not done, the correlation function can be seriously degraded and its shape changed from the predicted form, since the phase of the light traveling the longest paths is randomized by the loss of coherence rather than by the particle motion. The laser beam was focused onto

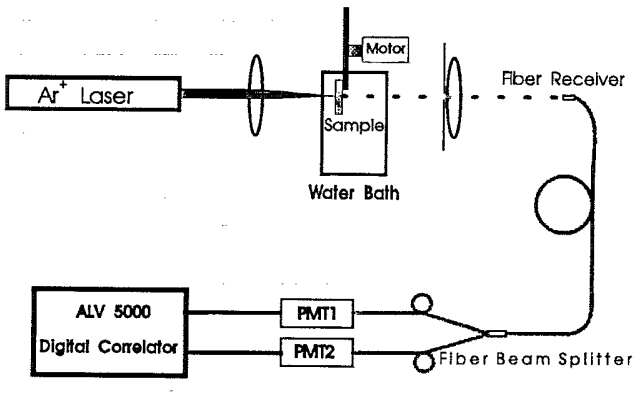

FIG. 4. Schematic diagram of experimental setup.

one side of the sample, and the light was collected from the other side. The laser power incident on the sample was typically about 100 mW, and was adjusted for the different samples to attain sufficient count rates for each.

The scattering cells were thin optical cuvettes, 1 cm wide. Thicknesses of 1, 2, or 5 mm were used, with the choice dictated by ensuring that $L/l^* > 20$ so that the diffusion approximation could be safely applied, and so that boundary effects were minimized [25]. The samples were immersed in a water bath, which allowed the temperature to be maintained constant to within less than 0.1 K over the course of the measurements. This is essential to ensure that the viscosity does not vary over the course of the data collection. Immersion in the water bath also reduces the effects of internal reflections at the interface. Data for the larger spheres were all collected at room temperature; data for the smaller spheres were collected at an elevated temperature of about 40 ° C. This decreased the viscosity of the water, thereby increasing the characteristic hydrodynamic time scale, $\tau_0 = \rho a^2/\eta_0$, and allowing us to make measurements at shorter relative time scales.

To study the very fast time scales of interest, we used a cross-correlation technique [26]. The signal was divided into two equal portions, each of which was detected with a photomultiplier tube (PMT). The outputs of the two PMT's were cross correlated. This method reduces the deleterious effects of afterpulsing in the individual PMT's. Afterpulsing is caused by the generation of secondary pulses induced either by ionization of atoms inside the tube, or by emission of photons due to electron absorption on a dynode or on the anode. The occurrence of afterpulsing introduces a spurious correlation at short times when the signal from a single PMT is autocorrelated; this is greatly reduced by cross correlating the signals from two PMT's. The cross-correlation technique also reduces the effects of dead time in the PMT's and the electronics, since only the rising edge of each pulse triggers the counter in either channel. Provided that the count rate in each tube is not too large, this allows measurements to be made at significantly faster time scales than would be possible with a single PMT.

Our detection optics used either multimode or single mode optical fibers [27]. In both cases, the beam splitter was integrated into the fibers, greatly simplifying the alignment. The multimode fiber had a core diameter of 100 μm, and standard, two-pinhole optics were used to collect the light. The fiber aperture itself acted as one of the pinholes, and a lens imaged the fiber face onto the collection side of the sample. Thus, the fiber diameter determined the area over which the light was collected. A second aperture at the lens was adjusted to limit the range of scattering vectors collected by the fiber, thereby increasing the size of the speckle spot so that it matched the size of the fiber core; this ensured a relatively large value for the intercept, β, of the measured intensity correlation function. In some experiments, we used a single mode fiber, instead of the multimode fiber; in this case the light was collected by a graded index (GRIN) lens with a 0.25 pitch. The single mode fiber collects only the light incident on the face of the GRIN lens, which is in a single spatial mode. This results in an even larger intercept, β, while maintaining a high efficiency for light collection. Moreover, a single mode fiber receiver offers the possibility of working with an arbitrarily large scattering volume and with an arbitrary working distance.

The correlation functions were calculated using a correlator capable of measuring delay times as short as 12.5 ns. At longer times, the channels were spaced in an increasing geometric progression with delay time. This provided sufficient accuracy to measure the decay of the correlation function down to levels of about 10^{-4}. The very short delay times of the early channels made obtaining data with good statistical accuracy quite challenging. This problem was exacerbated by the need to maintain the count rate at a relatively low level to avoid dead-time problems in the cross-correlation technique. As a result, we typically collected data for about 12 h to obtain sufficiently good statistics at the shortest times. The correlation functions were collected in successive 10-min intervals, and the results were averaged. The samples were mounted on a motorized wheel, and the larger spheres were rotated and shaken every 10 min to minimize the effects of sedimentation.

V. EXPERIMENTAL RESULTS

In a DWS experiment, as in all dynamic light-scattering experiments, we measure time correlations in the intensity of the scattered light $\langle I(t)I(0)\rangle$. Since the average intensity is nonzero, $\langle I(t)I(0)\rangle$ does not decay to zero at long times, but to the square of the average value of the intensity, $\langle I\rangle^2$; thus we normalize the data to their long-time limit and obtain a normalized intensity autocorrelation function,

$$g_2(t) = \frac{\langle I(0)I(t)\rangle}{\langle I\rangle^2}. \tag{40}$$

Since the fluctuations in electric field are Gaussian, the fluctuations in intensity can be replaced by the square of the fluctuations in electric field (the Siegert relationship), allowing us to express $g_2(t)$ in terms of the normalized field autocorrelation function $g_1(t)$ [Eq. (35)]

$$g_2(t) = 1 + \beta|g_1(t)|^2; \tag{41}$$

β is the coherence factor, which determines the intercept of the data at zero delay time. The value of β depends on the optical arrangement used in the experiment and reflects the number of coherence areas detected; as the number increases, the modulation of the intensity, and thus β, decreases. For polarized scattering detected with a single-mode optical fiber, $\beta \approx 1$; for the typical two-pinhole receiver, β is somewhat less than 1. However, multiply scattered light is completely depolarized, and there is no correlation between the intensities of the two polarizations in a single speckle; thus the value of β is reduced by a factor of 2, so that $\beta \approx 0.5$.

A typical set of data, collected for about 12 h from a sample of 1.53-μm-diam spheres at a volume fraction of $\phi = 0.20$, is shown in Fig. 5; we plot $g_2(t) - 1$ versus

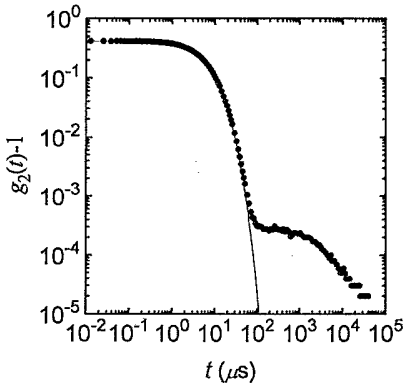

FIG. 5. A typical correlation function obtained in the DWS experiments for a 1-mm-thick sample cell containing 0.77-μm-radius polystyrene spheres at $\phi = 0.2$. The data were collected for about 12 h to improve the signal-to-noise ratio. The data have been normalized by the measured background, which is the square of the average intensity; this background has also been subtracted from the data. The solid line through the data is a fit to the functional form, scaled to the volume-fraction-dependent hydrodynamic time scale. The second decay at longer times is due to fluctuations in the laser intensity.

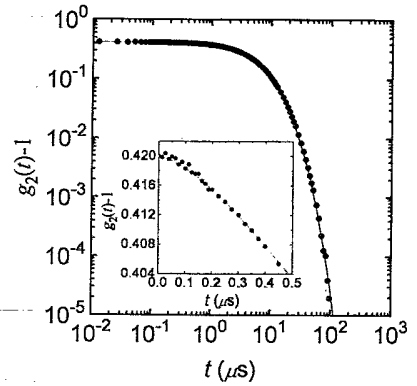

FIG. 6. The correlation function with the laser fluctuations subtracted. Over four decades of decay can be observed. The inset shows the first few data points on a linear scale, and demonstrates the absence of afterpulsing effects down to the shortest time scales. The fluctuations at the shortest time scale result from the very narrow sample times used and represent the largest noise in the data. The solid line through the data is a fit to the functional form, scaled to the volume-fraction-dependent hydrodynamic time scale.

time. The signal-to-noise ratio of the data is good enough that over two and a half decades of decay in the correlation function are observed. At longer times there is an additional correlation observed in the data, due to fluctuations in the laser intensity. Independent measurements of this correlation function were made, allowing the contributions of the laser fluctuations to be subtracted from the DWS data. This was done by fitting the contributions of the laser fluctuations to an exponential decay, and subtracting this from the data. The corrected correlation function is shown in Fig. 6; the subtraction procedure is sufficiently accurate that the corrected correlation function can be measured over more than four decades of decay.

The inset displays the data over the first 0.5 μs in a linear plot. It confirms the absence of afterpulsing effects, even down to the very short time scales accessible with our fast correlator and cross-correlation scheme. It also illustrates the level of the random fluctuations, or noise, in the data at the shortest time scales. This represents the largest fluctuations in the data because the time scale is so short; at longer times, these fluctuations are substantially reduced. The measured intercept is ≈ 0.42, somewhat less than 0.5 as expected for the two-pinhole, multimode optical fiber receiver used. The actual value of the intercept must be determined experimentally; for very short times (i.e., for small decays of the correlation function), the uncertainty in β is the limiting factor in the accuracy of the data. To determine the most reliable value of β, a smooth polynomial is fitted to the first few data points. The data are normalized by the fitted value of β and the electric-field correlation function, $g_1(t)$, is then obtained using Eq. (41). A zero crossing routine is used to invert the data, which are assumed to follow the equation for a point-source geometry, Eq. (38). From this inversion, we obtain t_D^* [Eq. (36)]. This is multiplied by $[S(q)]$, which is calculated using the Percus-Yevick equation for the structure factor [28] and the Mie-theory scattering results for the form factor (Fig. 3). The final result from this analysis is the DWS-averaged $[H(t)]$ defined in Eq. (34).

To set the absolute level of the $[H(t)]$ data, knowledge of the transport mean free path, l^*, is required. It can, in principle, be obtained by two independent methods: l^* can be calculated theoretically [29], using Mie scattering theory for the form factor and correcting for the particle correlations using the Percus-Yevick structure factor; alternatively it can be determined experimentally by a measurement of the static transmission through the sample [15]. The static transmission is proportional to l^*; by comparing the measured transmission with that through a reference sample of identical thickness, and in the same geometry, the value of l^* relative to the reference can be measured [30,31]. By using a sample of relatively low volume fraction, the value of l^* can be calculated with reasonable accuracy, allowing the unknown l^* at higher volume fractions to be determined. However, in practice, we find that either of these techniques can introduce experimental uncertainties of the order of 5% in the value of l^*, which translate into uncertainties of the order of 10% in the absolute magnitudes of $[H(t)]$ determined from the data. Thus, we instead determine the absolute level of the data by scaling its long-time asymptote to the expected value of $[H^\infty]$, which is calculated using the theoretical values for $H^\infty(q)$ [32]. This ensures that the data at the different volume fractions and particle sizes are normalized in a consistent fashion. The uncertainty in this method can be tested by comparing the resulting values of l^* with those obtained

from independent static transmission measurements and from a Mie scattering calculation. This comparison is shown in Fig. 7 for three different particle sizes. In all cases, the values of l^* obtained by these different procedures are in good agreement with one another. The largest discrepancies between the two experimental measurements of l^* (scaling $[H(t)]$ to the theoretical long-time asymptote $[H^\infty]$ and static transmission data) are within about 5%, consistent with the experimental uncertainties in the measurements. The discrepancies with the Mie scattering theory are somewhat larger, as much as 30% in the worst case. We conclude that this scaling procedure provides a consistent method for determining $[H(t)]$, without introducing further uncertainties resulting from additional experiments.

The measured $[H(t)]$ are shown in Fig. 8 for several different particle sizes, and for a series of different volume fractions. The values of $[H(t)]$ are normalized by D_0, the limiting value of the diffusion coefficient at low volume fractions. The data are plotted as a function of the normalized time scales, t/τ_0, where $\tau_0 = \rho a^2/\eta_0$ is the viscous relaxation time of the suspension at low volume fractions. We are able to probe much shorter reduced times using larger particles; for the smallest particles, we can collect data only at times greater than several τ_0, even though we have reduced the viscosity of the suspension by making the measurements at an elevated temperature. The dashed line in each figure represents the behavior expected for a single particle in the fluid [12]. It includes the effects of the hydrodynamic interactions between the particle and the fluid, and thus approaches the asymptotic value very slowly, reflecting the algebraic decay of the velocity correlation function. The data for the lowest volume fractions follow this curve for all the different particle sizes; however, for the smallest particles, it is necessary to go to extremely low volume fractions (0.5%) to obtain agreement with the single-particle theory. At higher volume fractions, the data have lower asymptotic values, as expected; they also deviate from the single-particle curve at successively shorter times as the volume fraction is increased. However, in all cases, the data approach their asymptotic values rather slowly.

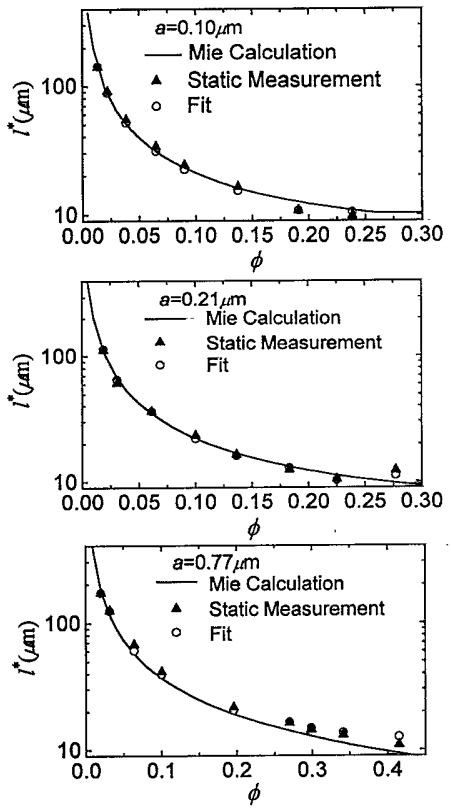

FIG. 7. Comparison of the values of l^* obtained by fitting the measured data to ensure that $[H(t)]$ goes to the expected value at long times (circles) with those values obtained by independent static transmission measurements (triangles) and with calculations based on Mie scattering and a structure factor calculated from the Percus-Yevick equation (line). The small deviations reflect the uncertainties inherent in each of these approaches, and confirm the validity of adopting the procedure of determining l^* from the fit of the data to the long-time value.

The most remarkable feature of the experimental data is that, for all volume fractions and for all sphere sizes, the measured $[H(t)]$ can be scaled onto a single master curve [8]. The functional form of this curve is given by the time-dependent mean-square displacement of an isolated sphere, $H_0(t^*)$, which can be calculated analytically [Eqs. (3) and (4)] [12]. The scaling of the experimental data is shown in Fig. 9 for the same set of particle sizes. For the largest size shown, $a = 0.77$ μm, the experimental data are not sensitive to the interaction portion of $[H(t)]$, and thus reflect the time-dependent mean-square displacement of individual particles. By contrast, the data for the smaller spheres are sensitive to the interaction contribution to $[H(t)]$, and thus the data can no longer be interpreted in terms of the mean-square displacement, but rather represent an average over time-dependent collective diffusion coefficients at various wave vectors.

The scaling of the data for the smaller spheres was unexpected; the measured $[H(t)]$ reflects a sum of two contributions, one from the self-correlations $H(t)$, and a second from the interparticle hydrodynamic interactions, $H_I(q,t)$. The data for large spheres measures the self-correlation $H(t)$ only, and this can be scaled to the master curve. There is no reason to expect the interaction contribution to have the same functional form as $H(t)$; in fact it has a quite different time dependence (see Sec. VII B). Nevertheless, the sum of the two contributions does scale to the same master curve; however, the scaling times, $[\tau(\phi)]$, are different for the different particle sizes. The ϕ dependence of these scaling times, normalized by τ_0, is shown in Fig. 10 for all the different particle sizes. The scaling times exhibit a pronounced dependence on both volume fraction and particle size. The data for the largest spheres follow the inverse of the ϕ-dependent, high-frequency viscosity [9], $\eta_0/\eta(\phi)$, as shown by the solid curve in Fig. 10. However, for a given volume fraction, $[\tau(\phi)]$ decreases rapidly with decreasing particle size. Even at very low volume fractions

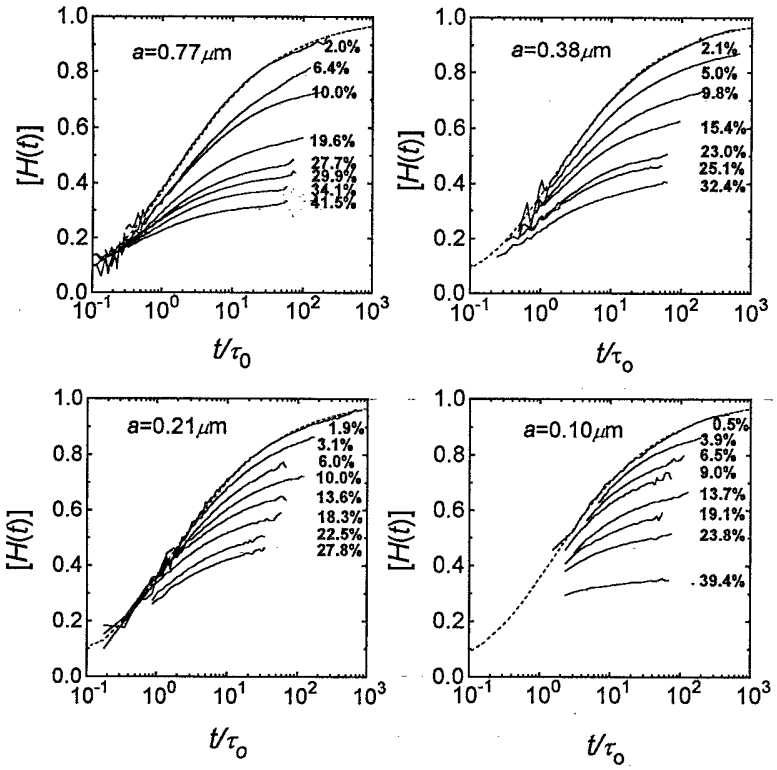

FIG. 8. Measurements of $[H(t)]$ for four different particle sizes and for several volume fractions for each. The data are plotted as a function of time normalized by the hydrodynamic time for each particle. The dashed lines are the theoretical prediction for a single particle at very low volume fractions; interparticle hydrodynamic interactions cannot affect this behavior. The data for the lowest volume fractions are in good agreement for all particle sizes. The data for the larger spheres were obtained at room temperature, while those for the smaller spheres were obtained at an elevated temperature, to increase τ_0, and thereby access earlier normalized time scales.

$[\tau(\phi)]$ is still sensitive to particle size; only at volume fractions $\phi < 0.5\%$ is it independent of particle radius.

The fact that the small sphere data scale in the same way as the large sphere data suggests that the approximation of a single relaxation time is still valid, independent of particle size; in a single relaxation time approximation, $[\tau] = [H^\infty]\tau_0$. However, the scaling time $[\tau]$ measured in the DWS experiments for small particles is much shorter than would have been expected from experimental measurements of the wavelength-dependent diffusion coefficient [33]. Moreover, for the smallest particles, the measured relaxation time $[\tau(\phi)]$ is even smaller than the

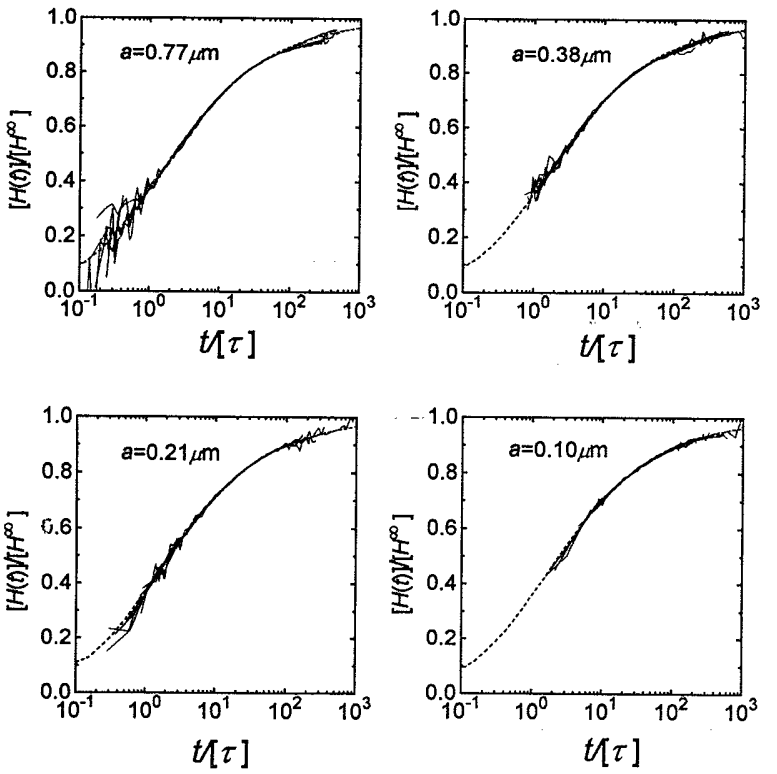

FIG. 9. Scaled $[H(t)]$ for four different sizes of spheres. The data for all volume fractions and for each sphere size collapse onto a single master curve, whose functional form is determined by the single sphere theory. The amplitudes of the data are normalized by the long-time value, $[H^\infty]$, and the times are scaled by a new, volume-fraction- and size-dependent scaling time $[\tau]$.

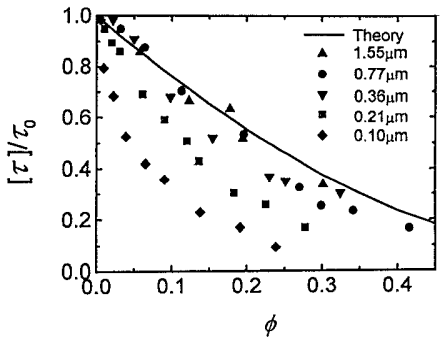

FIG. 10. Volume-fraction dependence of the measured scaling times for the different sizes of spheres. The scaling times are normalized by their values at $\phi = 0$, corresponding to the hydrodynamic time for each set of spheres.

$q = 0$ relaxation time, $H^{\infty}(0)\tau_0$, which is the shortest time we would have expected to measure. We discuss this point in more detail in Sec. VII D.

Since we have a simple analytic form for $[H(t)]$, we can both check and refine our data analysis by working backwards to the original experimental correlation function $g_2(t)$. Using the analytic form for $H_0(t^*)$ [12], and our values for the scaling time $[\tau]$, we calculate $g_1(t)$ directly from Eqs. (36) and (38). The correlation function $g_2(t)$, calculated using Eq. (41), can be compared with the original, and the intercept then adjusted to provide the best agreement with the data. We typically found that only small changes in β were required. An example of the quality of the fit to the original data is illustrated by the solid line shown in Fig. 6; clearly the agreement is excellent. We can also use this back calculation to check for the possibility of absorption. Although both water and polystyrene latex exhibit very weak absorption, the optical path lengths are sufficiently long that absorption can have some influence. The effects of absorption can be included in the back calculation of the correlation function, $g_2(t)$, by incorporating an absorption length [31]. However, we found that the data showed virtually no effects of absorption, and so the shapes of the correlation functions were not modified.

VI. SIMULATION METHOD

Numerical simulations have begun to make significant contributions to the study of particle suspensions, by incorporating accurate calculations of the low Reynolds number or creeping-flow hydrodynamic interactions between spheres [34,35]. Nevertheless, these methods are very expensive computationally, and cannot easily be applied to large systems. Moreover, extensions of these methods to time-dependent hydrodynamic interactions would be even more time consuming; it would be necessary to calculate the hydrodynamic interactions at many different frequencies and then take an inverse Laplace transform. Theoretical results for time-dependent hydrodynamic interactions are only available for dilute suspensions [36]. However, numerical algorithms based on discrete-velocity (lattice) gases [11,37] simulate the time-dependent Navier-Stokes equations directly, including thermal fluctuations; these techniques can therefore probe the temporal and spatial evolution of hydrodynamic interactions in complete detail. In this paper we use lattice Boltzmann simulations [6,7] to help interpret the DWS results. It may be that an improved understanding of these time-dependent interactions will lead to new and more efficient methods for computing time-independent (creeping-flow) hydrodynamic interactions.

The simulations used in this work are based on a combination of molecular dynamics, which is used to track the motion of the solid particles, and a fluctuating lattice Boltzmann model of the fluid. The motivation behind the development of lattice-gas and lattice Boltzmann models was the desire for a simplified molecularlike model of the fluid, which, although lacking some of the detailed mechanics of molecular dynamics, would still reproduce correct hydrodynamics at sufficiently large scales. It turns out that such models are remarkably effective at reproducing the hydrodynamic forces that occur in the dynamics of colloidal suspensions [7], although it has become apparent that the lattice Boltzmann equation is, by and large, a better simulation tool for hydrodynamics than lattice gases. However, in its normal state the lattice Boltzmann equation cannot model the molecular fluctuations in the solvent that give rise to Brownian motion. Nevertheless, on length scales and time scales intermediate between the molecular and the hydrodynamic, thermally induced fluctuations can be reduced to random fluctuations in the fluxes of the conserved variables [38]. In the present context, this means that the time evolution of the lattice Boltzmann velocity distribution includes a stochastic term representing the thermally induced fluctuations in the stress tensor [11]. These random stress fluctuations are uncorrelated in space and time and are sampled from a Gaussian distribution; the variance of the fluctuations serves to define the effective temperature of the fluid [38]. Numerical tests show that the resulting particle motions, in dilute to concentrated suspensions, closely match experimental results [9,10], even at very short times where particle inertia plays an important role. Since a detailed account of the algorithm has already been published [6], together with extensive numerical tests [7], this discussion will not be repeated here. Instead we will describe specific details of the calculation of time- and space-dependent hydrodynamic interactions.

Diffusing wave spectroscopy probes times that are very short compared with the time it takes a particle to diffuse a hydrodynamically significant distance; typical particle displacements are around 10^{-3} of the particle radius. We can most easily reproduce this situation on the computer by constraining the particle coordinates to their initial values. Thus the particles sit at fixed positions and interact hydrodynamically via fluctuations in translational and rotational velocity; in this case the long-time limit of $H(q,t)$ is related to the short-time wave-vector-dependent diffusion coefficient, $D(q)/D_0 = H^{\infty}(q)/S(q)$. However, we cannot measure particle displacements directly, as is done experimentally, since the particle coordinates are fixed. Instead we calculate $H(q,t)$ indirectly,

via its second derivative, the longitudinal velocity correlation function $J(q,t)$; from Eq. (10),

$$J(q,t) = \frac{d^2}{dt^2}[D_0 t H(q,t)] = \left\langle \frac{1}{N}\sum_{i,j=1}^{N} [\hat{\mathbf{q}}\cdot\mathbf{U}_i(t)\mathbf{U}_j(0)\cdot\hat{\mathbf{q}}]\, e^{i\mathbf{q}\cdot\mathbf{R}_{ij}} \right\rangle . \quad (42)$$

The initial value of the correlation function $J(q,0) = k_BT/M$, where M is the particle mass.

We calculate $J(q,t)$ from the particle coordinates and velocities, by averaging over 10^4 time steps, or about 500 times the typical relaxation time of the correlation functions. In addition, the simulations were run for 10^3 steps before any data were collected, to allow time for the hydrodynamic interactions to develop and for the particle velocities to come to thermal equilibrium. Since the particle configuration does not change during the course of the simulation, it is necessary to average over an ensemble of initial conditions, which were generated from a hard-sphere Monte Carlo program. Thus in addition to the time averaging, we also ensemble averaged each set of results over ten independent configurations. The statistical errors in $H(q,t)$ are of the order of 10% at long times and significantly less at shorter times; this is adequate for the present purposes. It would have been desirable to use more extensive ensemble averaging, say 100 configurations, but the computational demands would have been excessive. Simulations were run at volume fractions of about 5% (dilute), 25% (semidilute), and 45% (concentrated). The effects of varying particle size, particle mass, number of particles, and fluid viscosity have all been studied. A compilation of the parameters characterizing each run is reported in Table I. It should be noted that the variations in particle size reported in the simulations do not correspond to different physical systems; the different particle sizes affect only the numerical accuracy of the results [7].

For a direct comparison with experiment, we have simulated the DWS average $[H(t)]$ [Eq (34)] using the Mie scattering form factor $F(q,a)$ (see Fig. 3) appropriate to each particle size. In the simulated DWS average, the particle size enters only through the choice of form factor; it has nothing to do with the particle radius reported in Table I. The q^3 factor in Eq. (34) weights the average towards the high-q components of $H(q,t)$. Thus for sufficiently large particles, that is, for particles with a radius greater than about 1 μm, DWS probes only the motion of individual particles [the high-q limit of $H(q,t)$]. For smaller particles, the DWS average includes some of the collective motions as well.

A drawback of the current computer code is that it cannot simulate neutrally buoyant particles, but only rather massive ones ($\rho_R > 4$). This makes a comparison with the DWS data somewhat indirect, as we must scale both sets of data to different $H_0(t^*;\rho_R)$ functions, appropriate to the different mass ratios; the values of ρ_R for each simulation are shown in Table I (for the experimental data $\rho_R = 1.05$). The variation in ρ_R makes a noticeable difference to the shape of the $H_0(t^*;\rho_R)$ function; a rough idea of the differences can be obtained by comparing the curves plotted in Fig. 9 ($\rho_R = 1.05$) and Fig. 13 ($\rho_R = 10$). Although this difference in ρ_R means that we cannot compare simulation and experimental data directly, we can nevertheless still compare each to $H_0(t^*;\rho_R)$ using the appropriate value of ρ_R, thereby providing an effective comparison between simulation and experiment. Moreover, this has also allowed us to probe different physical systems and perhaps learn something new about hydrodynamic interactions (see Sec. VII D). The technical reason for the limitations on particle mass is that the velocities are updated explicitly, with information at one time step being used to calculate the velocities at the next time step. Such numerical schemes can be unstable if insufficiently damped; in the present context this leads to a stability criterion that sets a lower bound to the particle mass [7]. This problem can be corrected by using a more complicated implicit update of the particle velocities, which uses information from both old and new velocities; this is planned in future work.

TABLE I. Specification of the system parameters used in the computer simulations; the labels in Figs. 11 and 15 correspond to the entries below.

System	ϕ	N	a	ρ_R
1	0.050	128	1.54	8.7
2	0.243	128	2.61	10.0
3	0.243	1024	2.61	10.0
4	0.255	128	4.53	5.0
5	0.451	128	4.53	11.0
6	0.451	16	4.53	11.0
7	0.451	128	4.53	5.0

VII. SIMULATION RESULTS

Our simulations of the long-time hydrodynamic interactions, $H_N^\infty(q)$, show a significant dependence on system size, or number of particles, N. The deviations of $H_N^\infty(q)$ from the large system limit $[H^\infty(q)]$ arise from the spatially correlated flow fields of the periodic images; they are of order a/L or $(\phi/N)^{1/3}$. In previous work [39], it has been shown that a correction for the system size dependence of $H^\infty(q)$ in the $q = 0$ and $q \to \infty$ limits can be calculated analytically. In the Appendix, these results are generalized to arbitrary q; the final result for a system of N spheres is

$$H^\infty(q;\phi) = H_N^\infty(q;\phi) + 1.76 S(q;\phi)\frac{\eta_0}{\eta(\phi)}\left(\frac{\phi}{N}\right)^{1/3}, \quad (43)$$

where H_N^∞ is the simulation measurement. These corrections lead to consistent estimates of $H^\infty(q)$ over a range of system sizes from $N = 16$ spheres to $N = 1024$ spheres and over the whole range of volume fractions, from dilute to concentrated. We have used Eq. (43) to correct all our simulation data for $H^\infty(q)$; the results are shown in Fig. 11.

Dynamically, the data for finite systems $H_N(q,t)$ begin to deviate from the large-system limit at times of the order L^2/ν; beyond this time, vorticity generated by the periodic images interferes with the flow in the unit cell of interest and $H(q,t)$ asymptotes rapidly to $H_N(q)$. Thus the accessible time range over which reliable simulation data for $H(q,t)$ can be obtained is proportional to $N^{2/3}$. We have found empirically that systems of 128 spheres are sufficiently large to enable $H(q,t)$ to be calculated out to times of order $100\tau(\phi)$ which is the range of experimental interest; thus most of our simulations are for 128 spheres.

A. Wavelength-dependent diffusion coefficients

The long-time asymptote of $H(q,t)$ can be obtained from a single integral of the longitudinal velocity correlation function [Eq. (42)],

$$H^{\infty}(q) = \lim_{t\to\infty} H(q,t) = \lim_{t\to\infty} \frac{d}{dt}\,[tH(q,t)] = D_0^{-1}\int_0^{\infty} J(t)dt; \tag{44}$$

this integral asymptotes to H^{∞} much more rapidly than $H(q,t)$ itself. In Fig. 11 we show simulations of $H^{\infty}(q)$ and $D_0/D(q) = S(q)/H^{\infty}(q)$, for comparison with theory and experiment; the data have been corrected for finite-size effects as described in Eq. (43). The different symbols correspond to solid particles of different size and mass, and to systems with different numbers of particles. The parameters characterizing each simulation are described in Table I. Within the statistical uncertainties, the corrected data for $H^{\infty}(q)$ are independent of number of particles, particle size, and particle mass. The results are in quite good agreement with Beenakker and Mazur's theoretical calculation [32]. However there are some discrepancies at intermediate concentrations ($\phi = 0.25$), which is also the region with the largest errors in the theoretical calculations of the limiting cases of low q ($H^{\infty}(0)$)

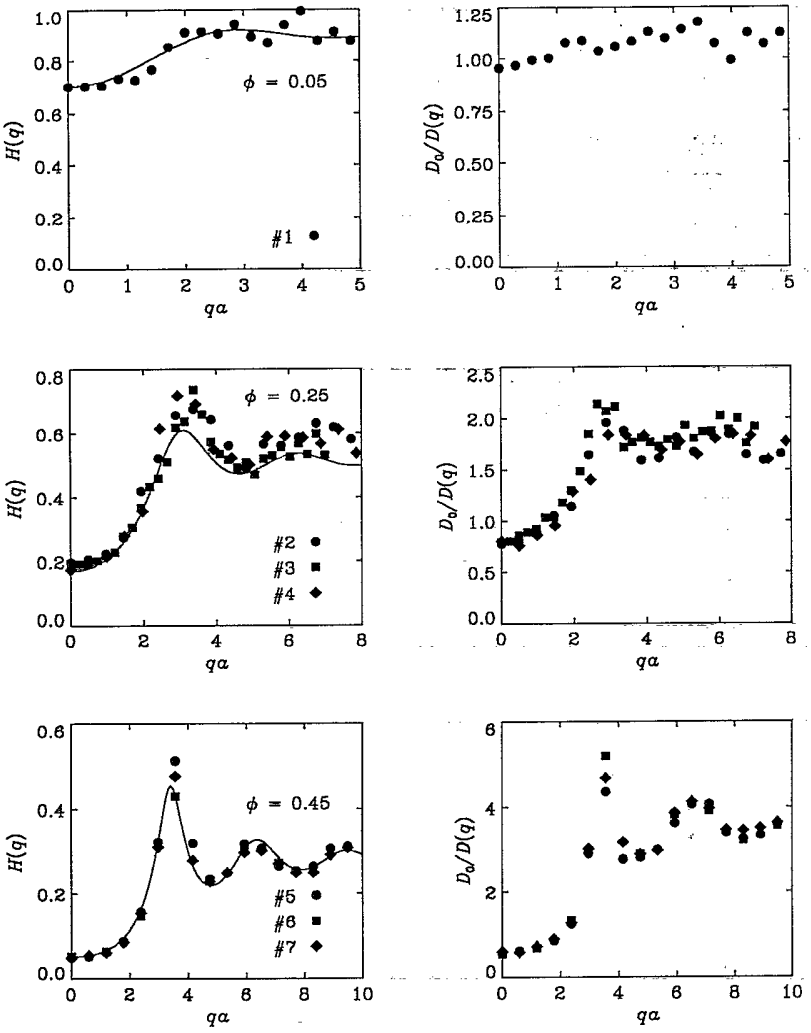

FIG. 11. Wavelength-dependent diffusion coefficients at various volume fractions. Simulation results for the function $H^{\infty}(q) = S(q)D(q)$ are shown as solid symbols. The different solid symbols correspond to different numbers of particles, particles of different mass, and particles of different size (with respect to the underlying lattice); the numbers correspond to the system parameters given in Table I. The solid lines are computed from theoretical work by Beenakker and Mazur [32]. Also shown are the inverse diffusion coefficients, $D_0/D(q)$ for comparison with experiment [33]. The symbols are the same as for the $H^{\infty}(q)$ plots.

and high q (H^∞). The simulation results are in better agreement with the known results [39]; the theoretical calculations are too small by 10%–20%. At high concentrations, both simulations and theory deviate from the correct results at high q [39] by 10%–20%; simulations with larger particles are necessary to completely capture the short-range hydrodynamic interactions at high concentrations. Results for $D_0/D(q) = S(q)/H^\infty(q)$ are also shown in Fig. 11, for comparison with experiment [33]. Again the agreement is quite good, but a detailed comparison is hindered by obvious uncertainties in both the simulation and the experimental data. However, the general behavior is similar; the peaks and troughs in $D_0/D(q)$ appear at the same values of qa and have quite similar magnitudes. The experiments would predict a higher first peak in $H^\infty(q)$ at $\phi = 0.45$, but this discrepancy is probably due mostly to the coarse sampling of qa in the simulations.

B. The interaction contribution $H_I(q,t)$

In Fig. 12 we show a small sample of our simulation results, for two characteristic wave vectors; $qa \approx 1.8$, a relatively long wavelength [Fig. 12(a)], and $qa \approx 3.6$, near the first peak of the structure factor [Fig. 12(b)]. The q dependence of the correlation functions is similar at all volume fractions, but more pronounced at higher concentrations; we show results at a volume fraction $\phi = 45\%$ to indicate the maximum variation with q. The scaled single-particle contribution, $H(t/\tau(\phi))/H^\infty(\phi)$, is indistinguishable from the theoretical curve for one sphere, shown in Fig. 12 by the solid line. By contrast, under these same scaling conditions, $H_I(q,t)$ exhibits very different behavior that is strongly dependent on q.

For small q ($qa < 2$) the interaction contributions are negative. At first sight this might be a little surprising; because of hydrodynamic interactions, the motion of one sphere tends to cause its neighboring spheres to move in the same direction. However, for sufficiently large volumes (i.e., for sufficiently small q), the average flow across any plane in the system must vanish. Thus, the motion of a particle induces a backflow of displaced fluid, which in turn sweeps the other particles along with it; this motion of particles and fluid opposes the motion of the primary sphere. Therefore, on sufficiently large length scales, there is an overall anticorrelation of particle velocities. By contrast, the wave vectors $qa \approx \pi$ probe primarily the first shell of neighbors; for such closely spaced particles the direct hydrodynamic interactions dominate the much weaker backflow effect, so that these contributions are positive. Finally, for very large q, there is no phase correlation between different spheres, and the interaction contribution vanishes.

C. Scaling of $H(q,t)$

The most remarkable result shown in Fig. 12 is that, although the interaction contributions (circles) do not scale to the single-sphere curve, the sum of the self-contribution and the interaction contribution at a particular wave vector (squares) *does* scale to the single-sphere curve, but with a different normalization, $H^\infty(q)$ rather than H^∞, and a different relaxation time $\tau(q)$. This is a general result, independent of q and independent of ϕ. An additional set of $H(q,t)$ data ($\phi = 0.25$, $N = 1024$) is shown in Fig. 13, to illustrate the scaling over the whole range of wave vectors. The wave vectors are proportional to the number of wavelengths, n, within the periodic unit cell $q = 2\pi n/L$ [the length of the unit cell $L = (4\pi N/3\phi)^{1/3}a$]; in this case (No. 3) $qa = 0.24n$ (Table I). Results for a system of 128 spheres are essentially identical for even values of n where the wave vectors are coincident. Simulations at other volume fractions show similar behavior and are not shown. Once again we see that the $H(q,t)$ data scale very well to the single-sphere master curve. There are deviations from scaling at small q ($n \leq 2$), but these are artifacts, which arise because the simulated systems are much more compressible than the experimental ones. As a result, the time scale for sound propagation, a/c_s (c_s is the speed of sound) is not negligible compared with the viscous time scales, $\rho a^2/\eta_0$; with the parameters chosen for these simulations, the dimensionless quantity $\rho c_s a/\eta_0$ is of order 10, whereas experimentally it is of order 1000. The simulated velocity correlation functions show a pronounced oscillation at low q, due to the effects of sound waves; the period of the oscillation is proportional to q [Fig. 14(a)]. These oscillations in the velocity correlations cause the deviations

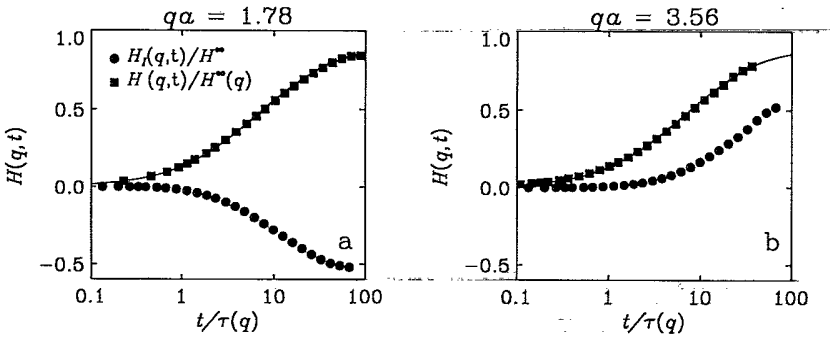

FIG. 12. Wavelength-dependent mean-square displacements at a volume fraction $\phi = 0.45$. Simulation data for $H(q,t)$ from a 128 sphere system (squares), normalized by the long-time asymptote $2D_0tH(q)$, have been scaled to the single-sphere curve by adjusting the relaxation time $\tau(q)$. The wave vectors are $qa = 1.78$ (a) and $qa = 3.56$ (b). The circles indicate the interaction contributions $H_I(q,t)$ at the two wave vectors, scaled in the same way as the single-particle correlation function $H_S(t)$.

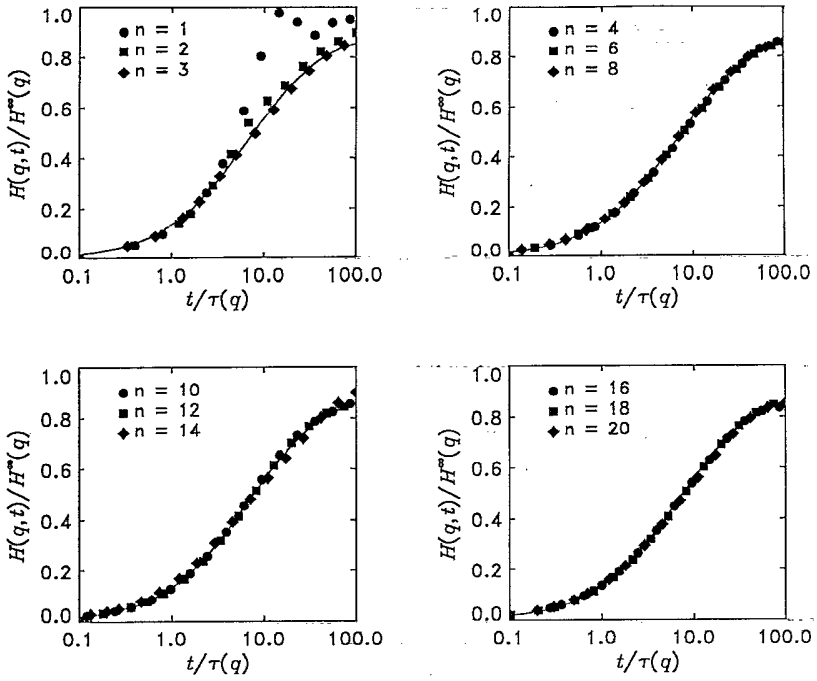

FIG. 13. Wavelength-dependent mean-square displacements at a volume fraction $\phi = 0.25$. Simulation data from a 1024 sphere system, normalized by its long-time asymptote $2D_0tH(q)$, has been scaled to the single sphere result by adjusting the relaxation time $\tau(q)$. The wave vectors are $qa = 0.24n$.

from scaling in $H(q,t)$ observed in Fig. 13. To confirm that these deviations are a compressibility effect, we have run a calculation with a much smaller viscosity, so that the ratio $\rho c_s a/\eta_0$ is now about 200. The velocity correlation function for this system is monotonically decaying at all q; an example is shown in Fig. 14(b). Thus for truly incompressible systems, we expect to see scaling of $H(q,t)$ over the whole range of length scales. It is also worth noting that these low-q correlation functions make next to no contribution to the DWS averages, since their weighting is very small.

The scaling of $H(q,t)$, observed in the simulations, implies that time-dependent hydrodynamic interactions can be characterized by a single time scale at each value of q, suggesting that the suspension is behaving as an effective medium at all length scales and at all time scales. The relaxation times required to scale the simulation data to the single-sphere master curve are shown in Fig. 15. The relaxation time scale is quite short at low q; it peaks around $qa = \pi$, and then, at large q, reaches the asymptotic value expected for the self-diffusion coefficient. The q dependence of the relaxation times is similar to the long-time asymptote $H^\infty(q)$ (Fig. 11), although there are noticeable deviations at small values of q ($qa < 1$); overall, this is reasonably consistent with a single relaxation time for $H(q,t)$.

We emphasize that this observed scaling is not a trivial result. Although $H(q,t)$ has very little structure, the overall fit is still sensitive to variations in system parameters. For instance, if one should attempt to scale $H(q,t)$ data to the single-sphere function for a particle with an incorrect mass density, no manner of adjustment of the relaxation time will produce a good fit. Although we do not claim that this scaling is necessarily exact over the whole time range, nevertheless, within the accuracy of both simulations and experiment we cannot detect any significant deviations from scaling.

The most important question is why should the data at various q scale onto the single-particle curve. We do not, as yet, have a complete explanation for these obser-

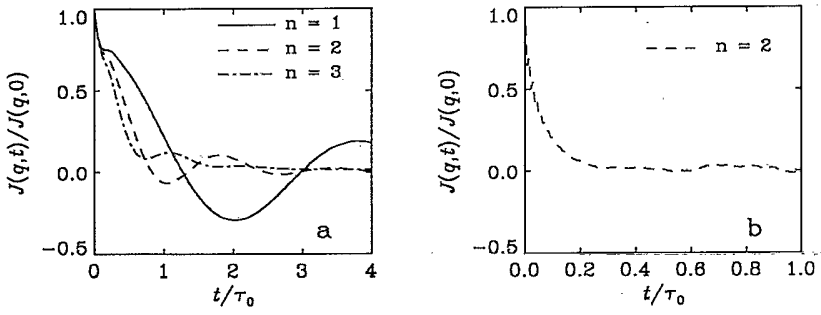

FIG. 14. Wavelength-dependent velocity correlation function $J(q,t)$ at a volume fraction $\phi = 0.25$. Simulation results from a 1024-sphere system are shown in (a) at various wave vectors $qa = 2\pi na/L = 0.24n$. Results from a system with a smaller viscosity are shown in (b). Since this simulation was for 128 spheres, there is only one coincident wave vector, $qa = 0.48$.

vations. At asymptotically long times the velocity correlation functions $\langle U_i(t)U_j(0)\rangle$ are known to decay with an algebraic $t^{-3/2}$ dependence, regardless of the separation between the spheres [40]. Thus any spatially weighted average of these correlation functions will also decay as $t^{-3/2}$ with some effective relaxation time [41]. However, the most interesting observation is that the correlation functions apparently see the same single-time-scale relaxation mechanism, regardless of spatial scale and concentration, modulated only by an effective viscosity $\eta(q,\phi)$; the origin of this is not understood.

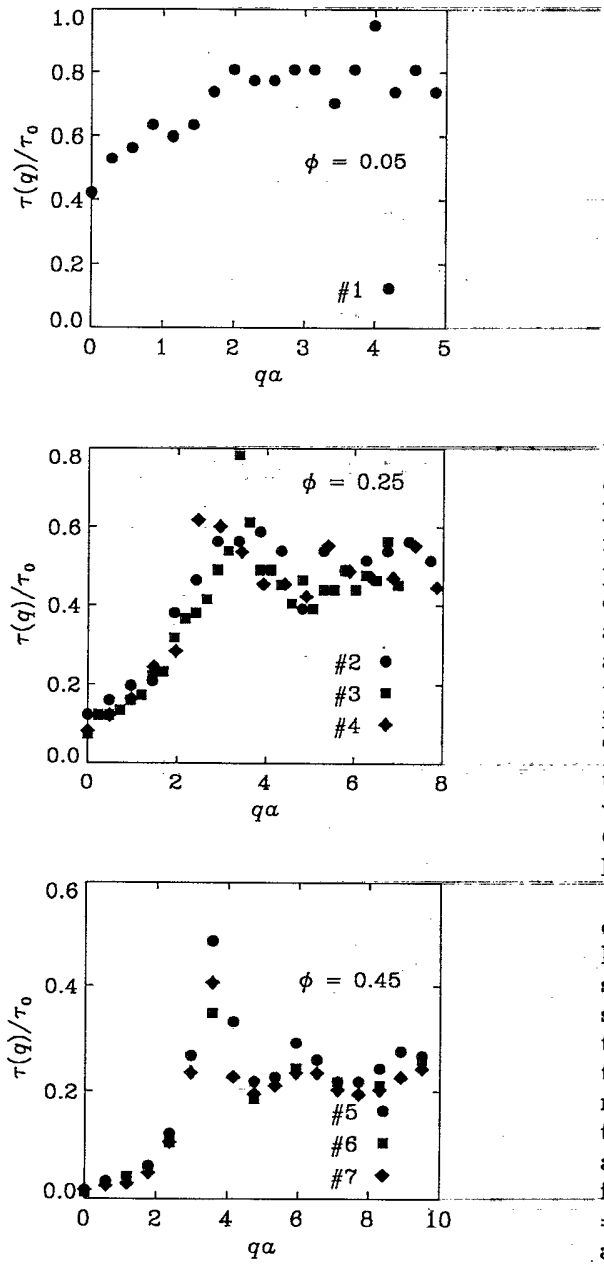

FIG. 15. Wavelength-dependent relaxation times $\tau(q)$, determined from plots similar to Fig. 13. The different solid symbols correspond to different numbers of particles, particles of different mass, and particles of different size (with respect to the underlying lattice); the numbers correspond to the system parameters given in Table I. In a single-relaxation-time approximation $\tau(q) = H^\infty(q)\tau_0$.

D. Scaling of $[H(t)]$

We have already observed that both the simulation data for $H(q,t)$ and the experimental data for $[H(t)]$ can be scaled to the single-sphere curve, $H_0(t^*;\rho_R)$, for the appropriate mass particles (see Sec. VI). This scaling is strikingly similar to our earlier observations for single-particle motion [9,11]. However, the effects of the collective hydrodynamic interactions are very evident in the behavior of the time scale, both in the experiments (Fig. 10) and in the simulations (Fig. 15). At a given volume fraction ϕ, the experimentally measured ratio $[\tau]/\tau_0$ decreases rapidly with decreasing particle size. At first sight, the monotonic decrease of the measured $[\tau]$ seems inconsistent with the variation in $\tau(q)$ shown in Fig. 15. To investigate the origin of this apparent discrepancy, we used the q-dependent simulation results to calculate the DWS-weighted average value, $[H(t)]$. We used the expected DWS weighting factors shown in Fig. 3 [5]. The behavior of the DWS-weighted simulation data is quite consistent with experimental observations; as shown in Fig. 16, the results for different particle sizes and different concentrations can again be scaled to the single-particle curve. The relaxation times, shown in Fig. 17, decrease monotonically with decreasing particle radius, as well as with concentration. Thus the pronounced variations in relaxation time with wave vector, observed in the simulations (Fig. 15), are washed out by the averaging over wave vectors inherent in the DWS experiment. The simulated DWS averages are insensitive to the details of the averaging process, and to the exact form of the weighting function; even using the asymptotic Rayleigh-Gans form factor instead of the Mie expression makes little difference to the result.

Although both the experimental and simulated $[H(t)]$ data scale to $H_0(t^*;\rho_R)$, the experimentally measured relaxation times (Fig. 10) for the smaller particles are much shorter (by about a factor of two) than predicted by the simulations (Fig. 17). We can make an independent estimate of the expected DWS relaxation times, based on the ratio of the integral of the longitudinal velocity correlation function $[H^\infty(q)]$ to its initial value k_BT/M; if there is a single dominant relaxation process, this equivalence is exact. We can therefore take experimental data for the wave-vector-dependent diffusion coefficient, $D(q) = H^\infty(q)/S(q)$ [33], and use it to estimate the DWS-averaged relaxation times. The resulting estimates of $[\tau]$ are close to the simulation results shown in Fig. 17 but quite different from the DWS-measured relaxation times. Moreover, for the smallest (0.1 μm) particles, the measured $[\tau]$ is even shorter than the $q = 0$ relaxation time, $H^\infty(0)\tau_0$, which is the shortest time one would have expected to observe. These considerations strongly suggest that there is an additional relaxation process in the DWS

experiments that is absent from the simulations. We believe that the excitation of collective motions of the particles by the scattering of sound waves may provide the extra relaxation mechanism. A quantitative theory for hydrodynamic interactions in a compressible fluid (i.e., including the propagation, scattering, and damping of sound waves) has not been developed as yet; even the theory for a single sphere is quite complex [42]. In the absence of a proper theory we suggest a mechanism, which seems to us to be physically reasonable, and which can account for the very short relaxation times observed in the experimental data for small particles.

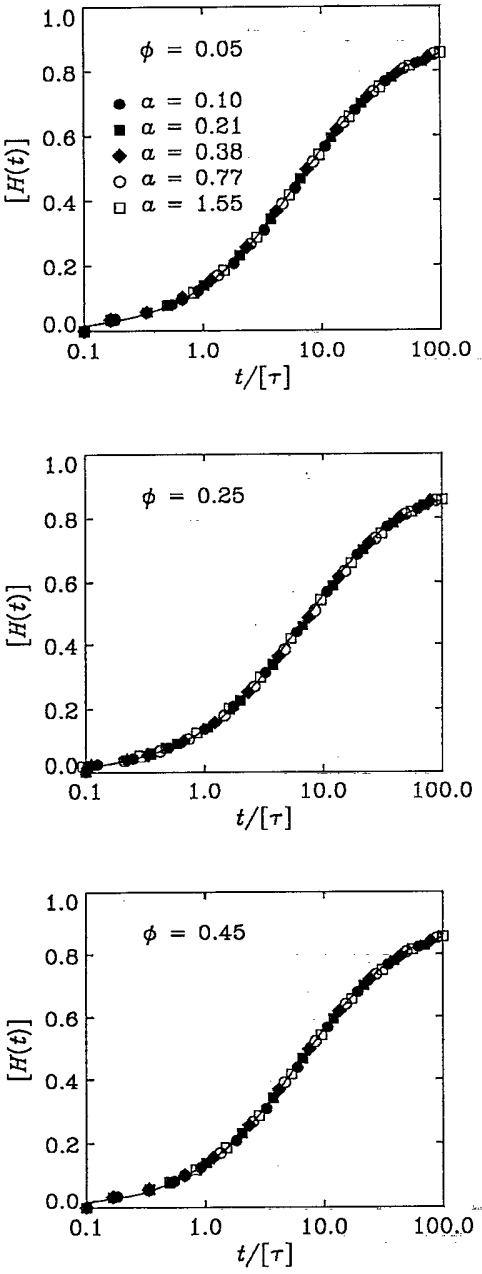

FIG. 16. Simulations of DWS correlation functions $[H(t)]$ for different sized particles. The simulation data for various wave vectors has been averaged over the appropriate weighting functions, as described in the text. The $H(q,t)$ data was taken from runs 1, 3, and 6 (see Table I).

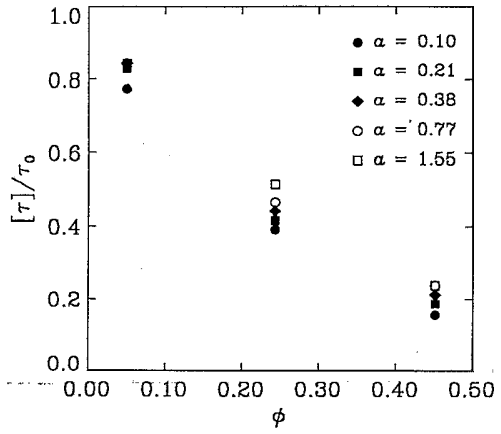

FIG. 17. DWS weighted relaxation times at various volume fractions. The data are taken from fits to the single-particle curve shown in Fig. 16.

When a sphere undergoes a fluctuation in its velocity, an impulse of momentum is transferred to the fluid. Part of this momentum impulse diffuses by viscous flow and gives rise to hydrodynamic correlations that require some time to take effect (of the order τ_0; see Fig. 12). However, additional momentum is carried off by sound waves, which causes a rapid decay of the particle velocity at very short times (of the order a/c_s). Thus, in a very dilute suspension, the velocity of a neutrally buoyant particle decays almost instantaneously from a root-mean-square value of $\sqrt{k_BT/M}$ to a smaller value of $\sqrt{2k_BT/3M}$ [43]. This rapidly decaying portion of the velocity correlation function makes no contribution to the mean-square displacement, and simply rescales the initial value (see Sec. II). In more concentrated suspensions the sound waves are scattered by neighboring particles, inducing collective motions at very short times; we have observed this effect visually in some two-dimensional computer simulations. Thus the velocities of *different* spheres can be correlated by sound propagation even at very short times, $t \approx a/c_s \ll \tau_0$. The effect of the scattered sound waves on the test sphere would be negligible, as only a tiny fraction of the initial momentum would be scattered back to the original location. Thus we would not expect the sound waves to significantly alter the shape of the self-correlation function, $H(t)$ (which dominates the large particle data), but only the collective correlations, $H_I(q,t)$, probed by the smaller particles.

The sound waves should perturb the collective particle motions until they are damped out by viscous dissipation, roughly on a time scale $\tau_0 = \rho a^2/\eta_0$. Thus the scattering of sound waves from particle to particle would produce additional contributions to $H(q,t)$ at small q and at short times. At longer times, the sound waves would be damped out; eventually we expect the mean-square displacement to track the incompressible fluid result. The overall effect of the sound waves would then be to in-

crease the measured values of $[H(t)]$ for small particles and at short times. Because the experimental measurements of $[H(t)]$ for small particles are so flat (see Fig. 8), and because the absolute amplitudes are not well known, a relatively small change in the short-time behavior of $[H(t)]$ (i.e., for times less than τ_0) could have a large effect on the estimated relaxation time.

This picture satisfactorily accounts for the main qualitative features of our observations. The primary difference between the experimental and the simulated systems is the mass density of the particles. In the DWS experiments they are nearly neutrally buoyant (minimizing sedimentation effects), whereas in the simulations the particles have a much larger mass density than the surrounding fluid. This provides a possible explanation for the discrepancy between the simulated relaxation times and the experimental measurements. The total momentum carried off by sound waves is independent of particle mass; it depends only on the mass of the equivalent volume of fluid. Thus for particles with mass densities much larger than the surrounding fluid (as in the simulations) this effect is small and almost all the momentum transfer is by viscous flow. However, for neutrally buoyant particles (as in the experiments), the momentum in the sound waves is a significant fraction of the total (1/3) and there are instantaneous correlations in particle velocities that are essentially absent for the more massive spheres used in the simulations.

There is another possible source of the discrepancy in the simulated and measured relaxation times. As we noted earlier (see Sec. IV), a small number of pairs of particles may lie within the range of the screened Coulomb potential. There are approximately $8\pi N^2 a^2 \lambda g_c/V$ such pairs, where λ is the screening length and g_c is the value of the pair distribution function at contact. These pairs of particles will repel each other electrostatically as long as they remain within the screening length; the interaction time t_λ is of order $\lambda\sqrt{m/k_BT}$, assuming the particle motion is ballistic in this time regime. Estimating the screening length as $\lambda = 50$ Å gives an interaction time $t_\lambda \approx 0.2$ μs for the 0.1-μm spheres; this is in the appropriate time range to modify the measured $[H(t)]$ at short times. We can also estimate the magnitude of the possible correction to the mean-square displacement. A pair of particles within the screening length will exert a force on one another of order k_BT/λ; over the interaction time, this produces an additional displacement of order $(k_BT/2m\lambda)t_\lambda^2 \approx \lambda$. Multiplying this mean-square displacement (λ^2) by the estimated number of interacting pairs, we can estimate that the correction to $[H(t)]$ is of order $\lambda^3/aD_0t_\lambda \approx \lambda^2\eta_0/\sqrt{mk_BT}$. This factor is of order unity for the smallest particles. For the larger particles, the effect is much less pronounced. The magnitude of the correction scales as $a^{-3/2}$ and the time scale over which it operates is proportional to $a^{3/2}$. Thus changes in the shape of $[H(t)]$ due to electrostatic interactions scale as a^{-3}.

VIII. CONCLUSIONS

In this work we have shown that the scaling relations first observed for the self-diffusion coefficient [9,11] apply to collective diffusion as well. Computer simulations show that the wave-vector-dependent diffusion coefficient has the same functional dependence on time for all wave vectors and at all solid volume fractions. These results suggest that monodisperse suspensions behave hydrodynamically as continuous media, over a substantial range of space and time scales, with only a varying effective viscosity. The characteristic time that scales the simulation data for the diffusion coefficient has a qualitatively similar dependence on wave vector to the structure factor of the suspension. The validity of the computer simulations was examined by a detailed comparison with diffusing wave spectroscopy experiments, which are sensitive to particle motions at the very small length scales and time scales required to observe the temporal evolution of the hydrodynamic interactions. The effective diffusion coefficient probed by the light scattering reflects an average over many wave vectors; however, by using particles of different sizes, the contributions from smaller wave vectors can be measured. Again the time-dependent data are found to scale to the same single-sphere functional form, with the characteristic scaling time decreasing with decreasing particle size, reflecting the larger contribution from the smaller wave vectors. A detailed comparison of wave-vector-averaged simulation data, weighted to match the light scattering, exhibits the same qualitative trends as the experiment; however, differences in relaxation time persist. We believe that these differences suggest that sound wave propagation may play an important role in the development of hydrodynamic interactions.

ACKNOWLEDGMENTS

We thank Patrick Warren, Pep Espanol, Rudy Klein, Scott Milner, Dave Pine, and Paul Chaikin for useful discussions. This work was partially supported by NASA and by the U.S. Department of Energy and Lawrence Livermore National Laboratory under Contract No. W-7405-Eng-48.

APPENDIX: FINITE-SIZE EFFECTS

At long times, the hydrodynamic interactions between spatially fixed (or very slowly moving) particles can be computed from the quasistatic or "creeping-flow" fluid equations [44]. The velocities of the spheres $\mathbf{U}_i$ are linearly related to the forces $\mathbf{F}_j$,

$$\mathbf{U}_i = \sum_{j=1}^{N} \boldsymbol{\mu}_{ij}\mathbf{F}_j; \tag{A1}$$

the mobilities $\boldsymbol{\mu}_{ij}$ are dependent on the configuration of all N spheres in the system. For a single sphere $\mu_0 = (6\pi\eta_0 a)^{-1}$. The hydrodynamic interaction function $H^\infty(q)$ is given by an ensemble average of $\boldsymbol{\mu}_{ij}$ [32]

$$\mu_0 H^\infty(q) = \left\langle \frac{1}{N} \sum_{i,j=1}^{N} \hat{\mathbf{q}} \cdot \boldsymbol{\mu}_{ij} \cdot \hat{\mathbf{q}} e^{i\mathbf{q}\cdot\mathbf{R}_{ij}} \right\rangle. \quad \text{(A2)}$$

It describes the average response of the system $\langle U(q) \rangle$,

$$\langle U(q) \rangle = \left\langle \frac{1}{N} \sum_{i=1}^{N} \hat{\mathbf{q}} \cdot \mathbf{U}_i e^{i\mathbf{q}\cdot\mathbf{R}_i} \right\rangle, \quad \text{(A3)}$$

to a spatially periodic external force $F(q)$,

$$\mathbf{F}_j = \hat{\mathbf{q}} F(q) e^{-i\mathbf{q}\cdot\mathbf{R}_j}; \quad \text{(A4)}$$

from Eqs. (A1)–(A4)

$$\langle U(q) \rangle = \mu_0 H^\infty(q) F(q). \quad \text{(A5)}$$

For a very dilute suspension, $H^\infty(q) \to 1$ at all q. However, for a periodic system, $H_N(q)$ differs from 1 by terms proportional to a/L (L is the length of the unit cell). The coefficient can be calculated by summing the flow fields from an infinite cubic array of spheres [45]; the correction to $H_N^\infty(q)$ is given by [39]

$$H^\infty(q) = H_N^\infty(q) + 1.76(\phi/N)^{1/3} + O(\phi/N). \quad \text{(A6)}$$

Except for very small systems, terms of order ϕ/N can be ignored.

At higher volume fractions, the hydrodynamic interactions between a sphere and its periodic images are screened by the other particles in the suspension. Since these interactions are at distances of order $L \gg a$, the screening can be accounted for by an effective medium, with viscosity $\eta(\phi)$ [46]. Thus if a force is applied to a particular sphere in a periodic system, that sphere experiences the flow field from all its periodic images, but modulated by the suspension viscosity, $\eta(\phi)$, rather than the pure fluid viscosity, η_0. This gives a correction to the high-q (single-particle) limit [39],

$$H^\infty = H_N^\infty + 1.76 \frac{\eta_0}{\eta(\phi)} (\phi/N)^{1/3}. \quad \text{(A7)}$$

It has been shown that this correction accounts for the system size dependence of the short-time self-diffusion coefficient, $D_S(\phi) = H^\infty D_0$ essentially exactly [39].

At longer wavelengths a particular test sphere sees not only the flow field from its periodic images, but also the flow field from images of neighboring spheres. We can approximate this flow field as an average flow field located at the image of the test sphere (sphere 1) but with an effective force [47].

$$\mathbf{F}_{\text{eff}} = \left\langle \sum_{j=1}^{N} \hat{\mathbf{q}} F(q) e^{i\mathbf{q}\cdot(\mathbf{R}_1 - \mathbf{R}_j)} \right\rangle = \hat{\mathbf{q}} F(q) S(q); \quad \text{(A8)}$$

$S(q)$ is the structure factor defined in Eq. (15). Thus our correction for $H^\infty(q)$, valid at all wave vectors and volume fractions, is

$$H^\infty(q) = H_N^\infty(q) + 1.76 S(q,\phi) \frac{\eta_0}{\eta(\phi)} (\phi/N)^{1/3}, \quad \text{(A9)}$$

as given in Eq. (43).

* Present address: Lawrence Livermore National Laboratory, Livermore, CA 94550.

[1] R. B. Jones and P. N. Pusey, Annu. Rev. Phys. Chem. **42**, 137 (1991).
[2] D. J. Pine, D. A. Weitz, P. M. Chaikin, and E. Herbolzheimer, Phys. Rev. Lett. **60**, 1134 (1988).
[3] D. A. Weitz, D. J. Pine, P. N. Pusey, and R. J. A. Tough, Phys. Rev. Lett. **63**, 1747 (1989).
[4] S. Fraden and G. Maret, Phys. Rev. Lett. **65**, 512 (1990).
[5] D. A. Weitz *et al.*, Phys. Scr. **T49**, 610 (1993).
[6] A. J. C. Ladd, J. Fluid Mech. **271**, 285 (1994).
[7] A. J. C. Ladd, J. Fluid Mech. **271**, 311 (1994).
[8] A. J. C. Ladd, H. Gang, J. X. Zhu, and D. A. Weitz, Phys. Rev. Lett. **74**, 318 (1995).
[9] J. X. Zhu *et al.*, Phys. Rev. Lett. **68**, 2559 (1992).
[10] M. H. Kao, A. G. Yodh, and D. J. Pine, Phys. Rev. Lett. **70**, 242 (1993).
[11] A. J. C. Ladd, Phys. Rev. Lett. **70**, 1339 (1993).
[12] E. J. Hinch, J. Fluid Mech. **72**, 499 (1975).
[13] I. Zúñiga and P. Español, Phys. Rev. Lett. **71**, 3665 (1993).
[14] D. A. Weitz and D. J. Pine, in *Dynamic Light Scattering. The Method and Some Applications*, edited by W. Brown (Clarendon Press, Oxford, 1993).
[15] J. Z. Xue, X. L. Wu, D. J. Pine, and P. M. Chaikin, Phys. Rev. A **45**, 989 (1992).
[16] J. X. Zhu, D. A. Weitz, and R. Klein, in *Photonic Band Gaps and Localization*, edited by C. Soukoulis (Plenum, New York, 1993).
[17] F. C. MacKintosh and S. John, Phys. Rev. B **40**, 2383 (1989).
[18] B. J. Berne and R. Pecora, *Dynamic Light Scattering with Applications to Chemistry, Biology and Physics* (Wiley, New York, 1976).
[19] P. N. Pusey and R. J. A. Tough, in *Dynamic Light Scattering: Applications of Photon Correlation Spectroscopy*, edited by R. Pecora (Plenum, New York, 1985).
[20] G. Maret and P. E. Wolf, Z. Phys. B **65**, 409 (1987).
[21] P. G. de Gennes, *Scaling Concepts in Polymer Physics* (Cornell University Press, Ithaca, 1979).
[22] X. Qiu *et al.*, Phys. Rev. Lett. **65**, 516 (1990).
[23] D. J. Pine, D. A. Weitz, J. X. Zhu, and E. Herbolzheimer, J. Phys. (Paris) **51**, 2101 (1990).
[24] M. Kerker, *The Scattering of Light* (Academic, New York, 1969).
[25] J. X. Zhu, D. J. Pine, and D. A. Weitz, Phys. Rev. A **44**, 3948 (1991).
[26] H. C. Burstyn and J. V. Sengers, Phys. Rev. A **27**, 1071 (1983).
[27] J. Ricka, Appl. Opt. **32**, 2860 (1993).

[28] W. Hess and R. Klein, Adv. Phys. **32**, 173 (1983).
[29] P. E. Wolf, G. Maret, E. Akkermans, and R. Maynard, J. Phys. (Paris) **49**, 63 (1988).
[30] A. Ishimaru, *Wave Propagation and Scattering in Random Media* (Academic, New York, 1978).
[31] D. J. Pine *et al.*, in *Scattering and Localization of Classical Waves in Random Media*, edited by P. Sheng (World Scientific, Singapore, 1990).
[32] C. W. J. Beenakker and P. Mazur, Physica (Amsterdam) **126A**, 349 (1984).
[33] W. van Megen, R. H. Ottewill, S. M. Owens, and P. N. Pusey, J. Chem. Phys. **82**, 508 (1985).
[34] J. F. Brady and G. Bossis, Ann. Rev. Fluid. Mech. **20**, 111 (1988).
[35] A. J. C. Ladd, J. Chem. Phys. **88**, 5051 (1988).
[36] H. J. H. Clercx and P. P. J. M. Schram, Physica (Amsterdam) **174A**, 325 (1991).
[37] A. J. C. Ladd, M. E. Colvin, and D. Frenkel, Phys. Rev. Lett. **60**, 975 (1988).
[38] L. D. Landau and E. M. Lifshitz, *Fluid Mechanics* (Addison-Wesley, London, 1959).
[39] A. J. C. Ladd, J. Chem. Phys. **93**, 3484 (1990).
[40] W. Van Saarloos and P. Mazur, Physica (Amsterdam) **120A**, 77 (1983).
[41] S. T. Milner and A. J. Liu, Phys. Rev. E **48**, 449 (1993).
[42] R. Zwanzig and M. Bixon, Phys. Rev. A **2**, 2005 (1970).
[43] E. H. Hauge and A. Martin-Löf, J. Stat. Phys. **7**, 259 (1973).
[44] J. Happel and H. Brenner, *Low-Reynolds Number Hydrodynamics* (Martinus Nijhoff, Dordrecht, 1986).
[45] H. Hasimoto, J. Fluid Mech. **5**, 317 (1959).
[46] C. W. J. Beenakker and P. Mazur, Physica (Amsterdam) **120A**, 388 (1983).
[47] T. Dodd, A. S. Sangani, D. A. Hammer, and D. L. Koch, J. Fluid Mech. **293**, 147 (1995).